

Contents lists available at ScienceDirect

Marine Structures

journal homepage: www.elsevier.com/locate/marstruc



Research paper

Design of a quick-connection device for installing pre-assembled offshore wind turbines

Behfar Ataei a,*, Zhengru Ren b, Karl Henning Halse a

- ^a Centre for Research-Based Innovation of Marine Operations (SFI MOVE), Department of Ocean Operations and Civil Engineering, Norwegian University of Science and Technology (NTNU), NO 6025, Aalesund, Norway
- ^b Institute for Ocean Engineering, Shenzhen International Graduate School, Tsinghua University, Tsinghua Campus, University Town, Shenzhen 518055, China

ARTICLE INFO

Keywords: Mating operation Quick connection device Finite element Offshore wind turbine

ABSTRACT

Higher wind velocities and lower wind shear are two motivations driving the development of floating offshore wind turbines (OWTs). However, such designs suffer from high expenses and complicated installation scenarios. Installation of offshore wind turbines is challenging due to the unpredictable nature of the environment and the technical complexities, especially at offshore sites. Mating of OWT on top of the pre-installed substructure is one of the critical stages of the installation operation. Grouted, welded, and bolted connections are utilized conventionally, but all have shortcomings. Welded and grouted connections suffer from fatigue forces, while a bolted connection requires minimal installation tolerances and sensitivity to impact forces. The design of a quick connection device (QCD) is expected to reduce the installation time, expand the operational weather window, and overcome the limitations of the earlier connection devices.

The QCD described here comprises conic cross-sections, circular plates, and stiffeners connected to the floating substructure and OWT. This research uses a global model to estimate the relative velocities and displacements between the OWT and spar buoy. Furthermore, a local finite element model is developed to assess the influence of the impact forces and the design of the connection device. Implementing the hydrostatic stiffness of the floating spar within the impact simulations improved the simulation fidelity and reduced the impact damage. Different impact scenarios are performed, and the sensitivity of impact damage concerning the distribution of impact initiation points is assessed. Furthermore, an active control mechanism is used to reduce the relative motions between the installation vessel and the floating substructure. It is concluded that utilizing the anti-swing active control system minimizes the impact velocity and impact damage. This research can be extended by optimizing the design of the quick connection device.

1. Introduction

Global energy consumption has reached more than 178,000 TWh in 2022 [1]. This number is only expected to increase, and providing sufficient energy will pose a significant challenge in the coming decades. In addition, societies and decision-makers are seeking to reduce fossil fuel consumption due to its negative environmental impacts. The United Nations has introduced a climate

E-mail addresses: behfar.ataei@ntnu.no (B. Ataei), zhengru.ren@sz.tsinghua.edu.cn (Z. Ren), karl.h.halse@ntnu.no (K.H. Halse).

https://doi.org/10.1016/j.marstruc.2024.103720

^{*} Corresponding author.

B. Ataei et al. Marine Structures 100 (2025) 103720

action to reduce the emission of greenhouse gasses by half by 2030 and to zero by 2050 [2]. These goals will not be realized until significant shifts are made toward utilizing renewable energies such as wind.

Offshore wind turbines (OWTs) have advantages compared to the onshore turbines, such as higher wind velocity and lower wind shear [3]. However, the OWT industry faces challenges, such as installation complexities and high expenses [4]. Attempts have been made to overcome these challenges by introducing innovative installation concepts; an example is the Centre of Research-Based Innovation, Marine Operations in Virtual Environments (SFI MOVE)'s design [5]. The design is of a low-height lifting installation concept where a pre-assembled OWT is installed with a single lift. To perform the mating operation offshore, there is a need for a connection device between the floater and the OWT, and the current connections do not have satisfactory performance.

The industry utilizes the grouted and bolted connections to connect OWT to the substructure. The grouted connections have issues with fatigue loads, and the connections are failing in less time than the systems were designed for [6,7]. In addition, these connections are unsuitable for offshore mating as the grout needs a substantial amount of time to harden. Meanwhile, the relative motion between the turbine and the substructure must be kept under 1 mm [8]. Utilizing bolted connections requires low tolerances during installation, which can be challenging during offshore operations. Furthermore, ensuring the bolts' tightness through the structure's lifetime is a challenge [9]. Other solutions exist, such as a slip joint, which is under development [10]. The slip joint concept utilizes two conic cross-sections forced into each other, and the load is carried by friction force. This article addresses the gap in the literature reflecting the lack of a suitable connection device.

Designing a suitable connection device requires examining both the global and local performance of the device. Rigid multibody dynamics are a suitable methodology for assessing global performance. The relative motion between the lifted OWT and floating substructure is a crucial input for designing a quick connection device (QCD), which we evaluate by performing the global analysis. As we have before [11], we perform the global modeling of the SFI-MOVE concept utilizing the Sima software [12]. In this work, we gave special attention to the effect of crane structural flexibility in addition to global modeling. Other than using state-of-the-art simulation tools such as Sima and Orcaflex [13], it is possible to code tailor-made simulation tools. In [14], a tailor-made simulation environment is developed in Matlab-Simulink, which gives flexibility to modeling any particular physics or phenomenon. This simulation environment was utilized for the development of multi-wire anti-swing control [15]. By using this control strategy we reduce the relative motions between the OWT and the substructure.

The impact between the objects can be modeled using the finite element method (FEM) [16]. In [17], FEM is utilized to assess the impact between the wind turbine blades and the hub. In this way, they were able to estimate the suitable wind velocity to perform the installation operation. Past research has used this methodology to address different impact scenarios of ship–ship [18], ship–bridge [19,20] or ship-fish farm [21]. Increasing the number of the bottom fixed and floating wind farms, the impact between the vessel and the substructure has also been discussed in the literature [22,23] using FEM.

This article proposes an initial design of a new connection device between the OWT and the substructure. In addition, it addresses how this device can assist in a successful installation operation using the low-height lifting mechanism. The global analysis assesses the relative velocities and alignment between the moving objects. An FE model of the quick connection device is developed, and the impact analysis is performed for different mating scenarios. The influence of considering the hydrostatic stiffness of the floater and implementing a control strategy is addressed.

The remainder of this paper is organized as follows: Section 2 presents different mating stages and introduces the quick connection device. Section 3 presents the simulation methodology for the global analysis (rigid multibody) and local impact analysis (FE). In Section 4, analyses are performed, and the results are discussed. In Section 5, the research is concluded, and recommendations for future research are presented.

2. Mating operation and quick connection device

2.1. Low height lifting mechanism

The SFI MOVE has introduced an installation concept that allows the installation of a pre-assembled OWT with a single lift, as shown in Fig. 1. This concept comprises a relatively small catamaran vessel equipped with a low-height lifting mechanism. The low-height lifting mechanism is composed of two 3D frame structures working as cranes, a collar, lifting and stabilizing wires, winches, and corresponding controllers. The OWT weight is carried from the bottom by lifting wires and stabilized from higher elevations by stabilizing wires. The collar moves freely alongside the OWT tower to ensure that the stabilizing wires do not contribute to the weight carried by the lifting wires. This concept enables the utilization of cranes with smaller heights compared to conventional methods, thus utilizing shorter cranes. In addition, this concept is less sensitive to the increasing large OWT sizes that the industry is adopting [24].

2.2. Mating stages

The operation aims to install the OWT on the top of the floating substructure. The mating operation consists of multiple sub-stages presented in Fig. 2:

- a Hovering phase: At this stage, the OWT hangs from the crane of the installation vessel as the approach to the substructure is not yet initiated. The global analyses in the current article are done at this stage.
- b Impact phase: At this stage, the OWT approach to the substructures is initiated, and the impact between the parts of the quick connection device occurs.

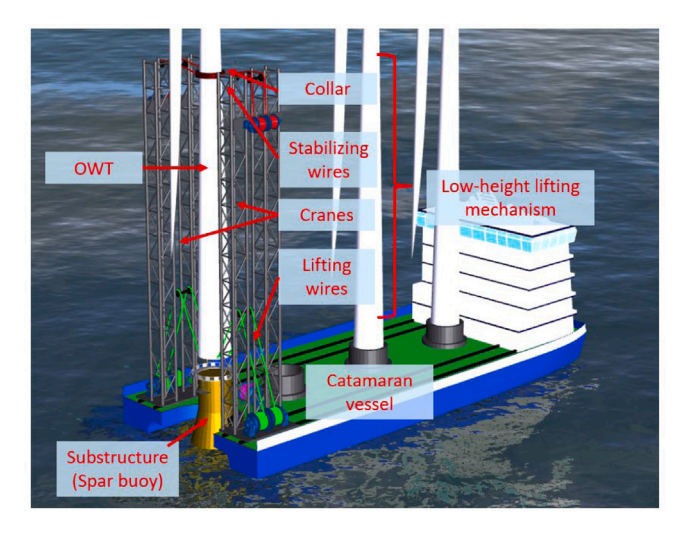


Fig. 1. Overview of SFI MOVE concept [5].

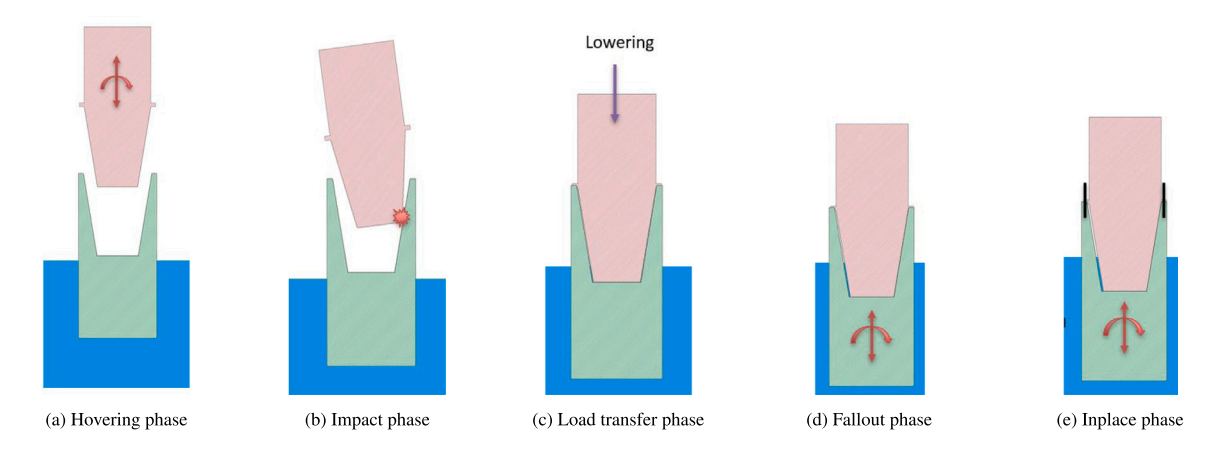


Fig. 2. Overview of mating operation stages.

- c Load transfer: The OWT weight is transferred from crane onboard the installation vessel to the floating substructure with constant velocity.
- d Falling out: At this stage, the OWT is placed on top of the spar, and the wires connections to the crane vessel are detached. The interaction between components of the quick connection device ensures the OWT stays on top of the substructure.
- e In-place: The final clamping is performed (if needed), and the OWT-spar assembly is ready for power production.

2.3. Operability of the mating operation

The operability of an operation is assessed by comparison of the target response with the acceptable limits recommended by the standards and industrial guidelines. The following responses are distinguished as the target responses:

- Relative motion between the OWT and the substructure: The excessive relative motion between the OWT and substructure
 results in unsuccessful mating.
- Plastic deformation during the mating: The extensive spread of plastic deformation results in repair work offshore. However, minor local dents might be acceptable.

The QCD is an innovative design that is in the early stages of development and the acceptable limits were not quantified. One of the objectives of this research is to quantify the limitations of the design, which can be utilized for the operability analysis.

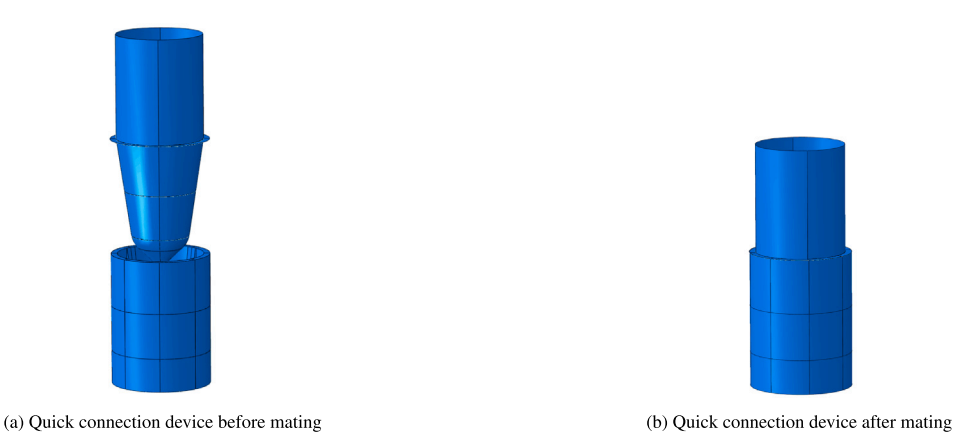


Fig. 3. Quick connection device before and after mating operation.

2.4. Quick connection device

One of the main problems the OWT industry is seeking to solve is the lack of a suitable device to connect the turbine and the substructure. This shortcoming is particularly critical during the offshore installation operation. The proposed quick connection device is expected to reduce the time required for the operation and increase the operational weather window. This device comprises two conic cross-sections installed on the OWT and the substructure. Fig. 3 shows this connection device before and after the mating is performed.

The quick connection comprises two structural assemblies at OWT and the substructure. In the proposed design, the assemblies are welded to both ends. At the OWT side, the quick connection device is connected to the tower by a top flange and is extended outward the OWT (see Fig. 4(a)). Four stiffeners penetrate the top flange to provide support for the conic cross-section. The cone offers a closed circumference for easier penetration to the substructure. In addition, it is designed with an axisymmetric shape for identical behavior in different directions. The conic cross-section and the stiffeners are welded together throughout the whole length.

At the substructure side, the quick connection device extends inside the substructure's outer tube. The conic cross-section, which is a partial cone, comprises eight impact plates. By not using a full cone at the substructure, we limit the friction force between two parts of the quick connection device. This enables easier detachment when it is needed for maintenance purposes. Behind each impact plate, a stiffener is inserted that connects the impact plates to the substructure outer tube. One top flange and end plate are located at the top and bottom of the connection device. The substructure end plate follows the shape of the OWT cone at the center. The top flange and cone at the OWT side are connected to the substructure top flange and end plate under the installed condition. The OWT cone and impact plates at the substructure side are also in contact.

3. Methodology

Three different models are developed to design the quick connection device. The first is the global model, where the effects of the hydrodynamic response of floating bodies and the low-height lifting mechanism are assessed. The second model is developed to evaluate the effect of impact forces in the local model utilizing FE methodology. Limitations are seen in implementing control methodologies in the simulation tools. Therefore, the control methodology is implemented in the third model, a tailor-made simulation environment developed in Matlab/Simulink [25].

3.1. Global analysis

To estimate the global system performance, multiple components of the system are assembled in the SIMA simulation tool [12]; see Fig. 5. SIMA is a workbench developed by the Sintef Ocean that enables maritime operations simulation.

The Hywind Scotland spar buoy [26] designed by Equinor is assumed to be the substructure in this research. The catamaran vessel and spar buoy are modeled with Simo rigid bodies. The hydrodynamic behavior of floating bodies is modeled using first-order wave response amplitude operators. The effects of slowly varying drift forces are assessed in a separate research study [27]. A dynamic positioning system performs vessel station-keeping, and the spar buoy uses three mooring lines. The detailed description of the numeric model is presented in [11].

The 3D frame crane structures are modeled using equivalent beams. These equivalent beams have the same flexural stiffness and displacement as the original frame structures. The calculation details of replacing the frame structures with equivalent beams are presented in [11]. In the global model, the equivalent cranes are modeled using Riflex beam elements, which have six degrees of freedom at each node (three translational and three rotational). The bottoms of the crane structures are coupled to the catamaran vessel reference point. Due to software limitations on modeling active control systems, winch controllers are not implemented in the

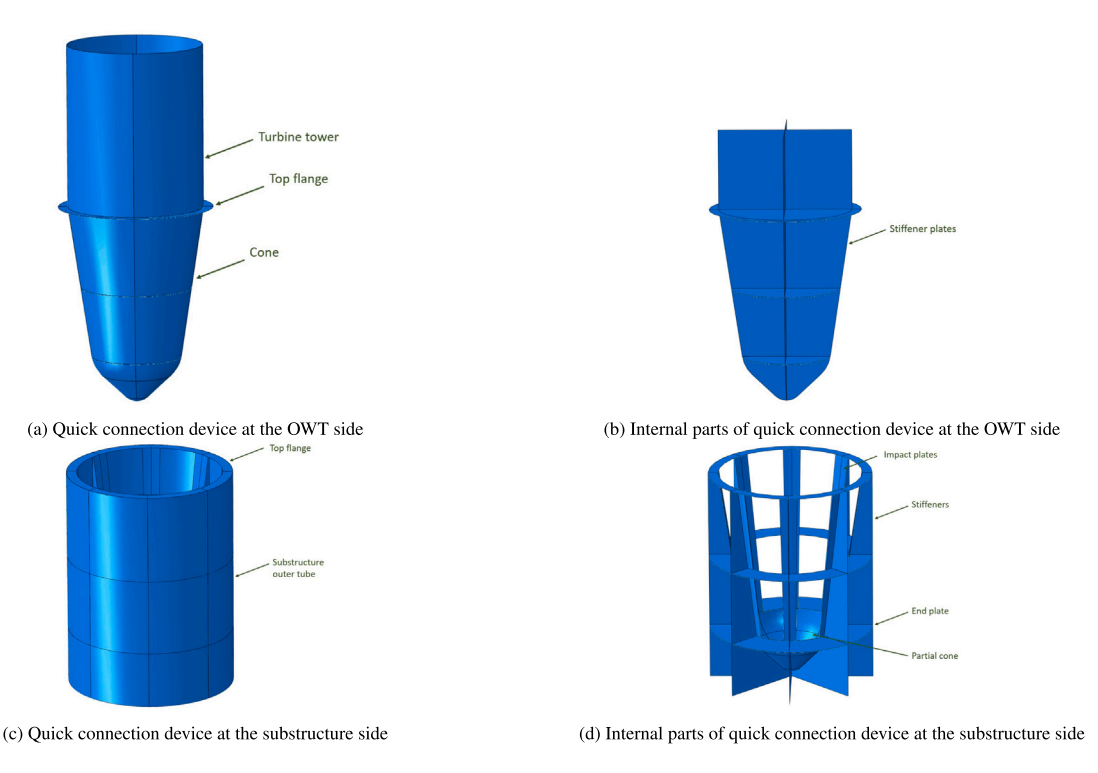
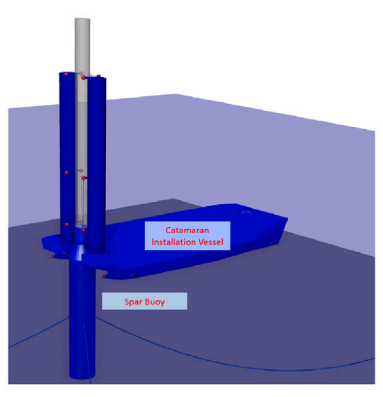
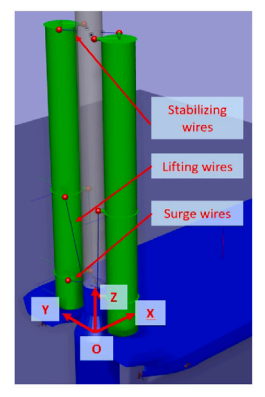


Fig. 4. Quick connection device connected to the OWT and substructure.



(a) Overview of global model in Sima



(b) Components of the low-height lifting mechanism model in Sima

Fig. 5. Overview of SFI-MOVE concept and SIMA model.

global model. The active control of the lifting lines in the original SFI-Move concept controls the horizontal and vertical motions of the bottom of OWT utilizing a multiple degrees of control algorithm. To replicate this control in the global model, the surge wires are added to limit the in-plane motions of the bottom of the OWT. The stabilizing wires work only on the horizontal plane and mainly take care of the OWT rotations. Lifting, stabilizing, and surge wires are modeled using tension-only wire elements, with one end connected to the lifting cranes and the other end connected to the hanging OWT. The DTU 10 MW Ref. [28] turbine is selected as the OWT and modeled using a rigid body hanging from the wires.

The main properties of the catamaran installation vessel, spar buoy, and OWT are summarized in Table 1.

The global analysis is performed for the irregular waves with significant wave height $H_s = 1$ m and varying peak periods $T_p = 6$, 8, 9, 10, 11, 12, 14, and 16 s. The Jonswap spectrum with the peakedness factor of $\gamma = 3.3$ is selected as the irregular waves spectrum [29]. The time-domain simulations are performed with a duration of 36000 s after the initialization, where transient responses have vanished.

Table 1
Main properties of the catamaran installation vessel, spar buoy, and OWT.

Object	Parameter	Unit	Value
	Length overall	m	144
	Breadth moulded	m	60
	Spacing between mono-hulls at waterline	m	38
Catamaran	Draft	m	8
Catalilalali	Displacement mass	tonnes	18503
	Vertical center of gravity above baseline	m	28.6
	Transverse metacentric height	m	66.4
	Initial position of reference point in global coordinate system	m	(63,0,0)
	Diameter at top	m	9.5
	Diameter at waterline	m	14
	Draft	m	70
Cman harass	Displacement mass	tonnes	11 045
Spar buoy	Vertical position of the center of gravity (COG)	m	-40
	Vertical position of the center of buoyancy (COB)	m	-35
	Vertical position of fairlead	m	-15
	Initial position of reference point in global coordinate system	m	(0,0,0)
OWT	Rated power	MW	10
	Number of blades		3
	Rotor diameter	m	178.3
	Hub diameter	m	5.6
	Hub height	m	119
	Rotor mass	kg	227,962
	Nacelle mass	kg	446,036
	Tower mass	kg	628,442
	Initial position of reference point in global coordinate system	m	(20,0,0)

3.2. Definition of coordination system

The global coordinate system is set to define the motion of the bodies. This coordination system, which follows the right-hand rule, is presented in Fig. 5(b). The origin of this coordination system is located at the spar centroid at the water plane. The X-direction is positive toward the north, and the Y-axis is pointed to the west. The Z-direction is defined upward. The floating objects (catamaran and spar) translation in X-, Y- and Z-directions are defined as surge, sway, and heave, and their rotations around the X-, Y-, and Z-axis are defined as roll (ϕ) , pitch (θ) , and $yaw(\psi)$.

3.3. Relative velocities

The relative motion between the two bodies comprises relative displacement (Δ) and relative alignment (δ). Relative displacement results from translational motion between the bodies, while the alignment comes from the angles between their center lines. The illustration of 2D relative displacement and relative alignment is presented in Fig. 6. If the operation is performed in the following sea condition, the governing responses are the global X- and Z-translations and rotation around the Y-axis. The impact forces for the design of the connection device are calculated based on the relative velocity between the OWT bottom and spar top and the relative angle between the two bodies.

3.4. Local FE model

To perform impact analysis, a local structural model is developed using the FE method; see Fig. 7. This model is created in the Abaqus tool developed by Dassault Systèmes [30]. The Abaqus is a state-of-the-art finite element tool with simulation capabilities for structural impact analysis.

Different components of the quick connection device are modeled using four-node linear shell elements (S4 elements); see Fig. 7(a)). These components include flanges, cones, stiffeners, plates and OWT and spar tubes in the vicinity of the connection device. The thickness of these structural components is more prominent than other dimensions; therefore, modeling the structure utilizing the shell elements is considered reasonable. Hourglassing [31] can occur when the elements are not fully defining the deformation shapes due to the lack of integration points. This results in deformed shapes that look like an hourglass when first-order or reduced-integration elements are utilized; it also results in increases in the solver's artificial energy. Therefore, full integration shell elements are used since hourglassing is expected to occur during the impact. Different parts of the model are connected by node sharing to compose the quick connection device.

Parts of OWT and spar tubes which are directly connected to the quick connection device are included in the FEM model. These parts are in the vicinity of the QCD; therefore, they might be influenced by the impact forces. The OWT and spar outside the impact region are modeled as rigid bodies with mass and inertia inserted at the center of gravity. The quick connection device at both sides is coupled to these nodes with kinematic couplings, including all six degrees of freedom (DOFs; see Fig. 7(b)). The contact between

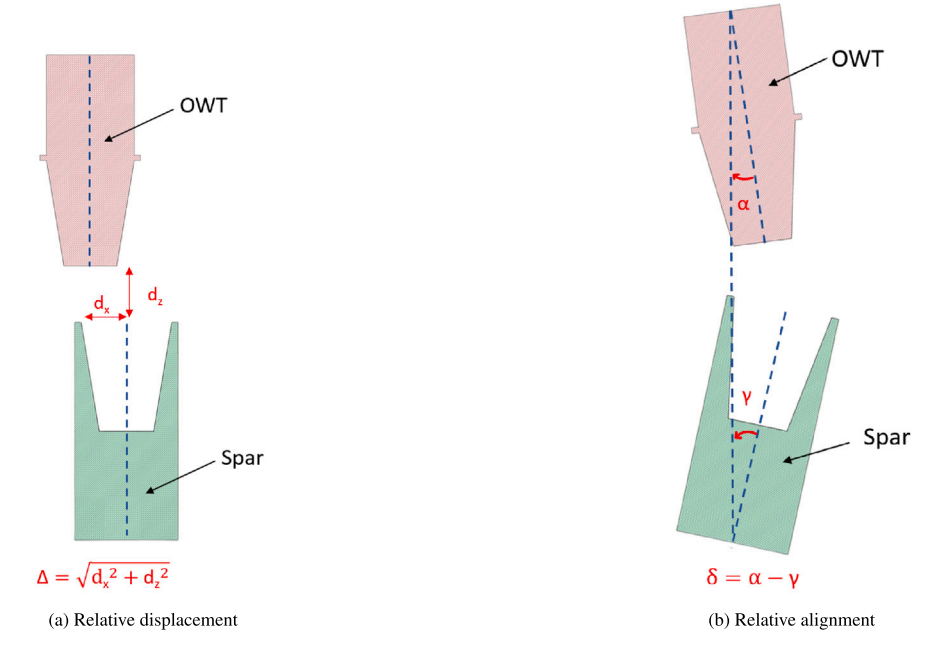


Fig. 6. Definition of relative displacement and relative alignment.

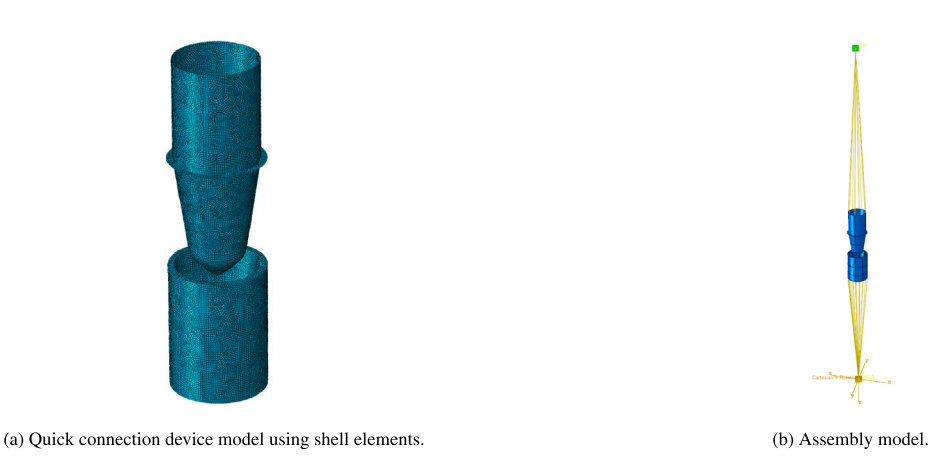


Fig. 7. Overview of FE model in Abaqus.

the components is modeled using a general explicit contact algorithm within the Abaqus tool. The tangential contact behavior is modeled as metal-to-metal friction with a force factor of 0.3. The normal direction of contact has hard behavior, which does not allow plates to penetrate each other.

3.4.1. Material properties

The steel grade S355J2 with a density of 7850 kg/m^3 is used as material for the connection device [32]. This material has a yield tension of 355 MPa, Young modulus of 210 GPa, and Poisson's ratio of 0.3. The plastic behavior of the material is defined with isotropic hardening and a bilinear stress–strain curve presented in Fig. 8.

The OWT's spatial location before the impact phase's initialization plays an essential role. This research assumes that the hovering phase ends when the vertical distance between the OWT and spar top is 2 m, and the impact phase begins as the OWT approaches the spar. Fig. 9 presents the spatial distribution of impact scenarios initiation points. The green dots demonstrate all alternative points where the QCD tip at the OWT side can be located at the beginning of the impact simulation. The operation is designed to be performed in restricted heading configuration with the following sea, which results in impact with the angle of $\beta = 0^{\circ}$ (see Fig. 9(b)). Furthermore, long-crested waves are utilized for environmental conditions and estimating relative velocities and alignment. However, some spreading influence is expected; therefore, in this stage, impacts with directions of $\beta = 22.5^{\circ}$ and 11.25° are selected in addition to 0° .

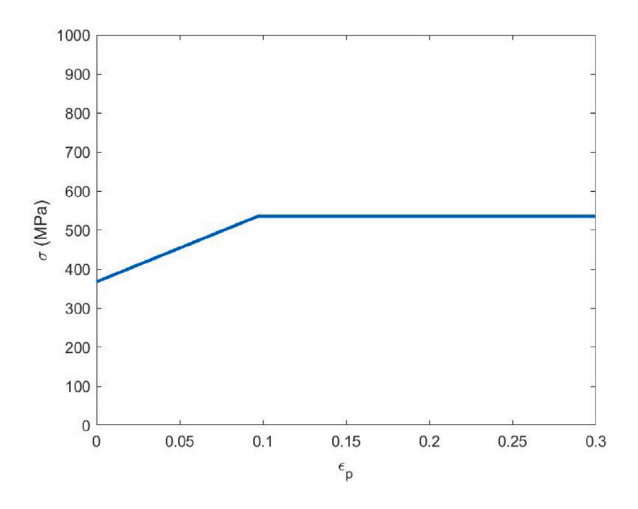


Fig. 8. The S355J2 steel material plastic stress-strain curve.

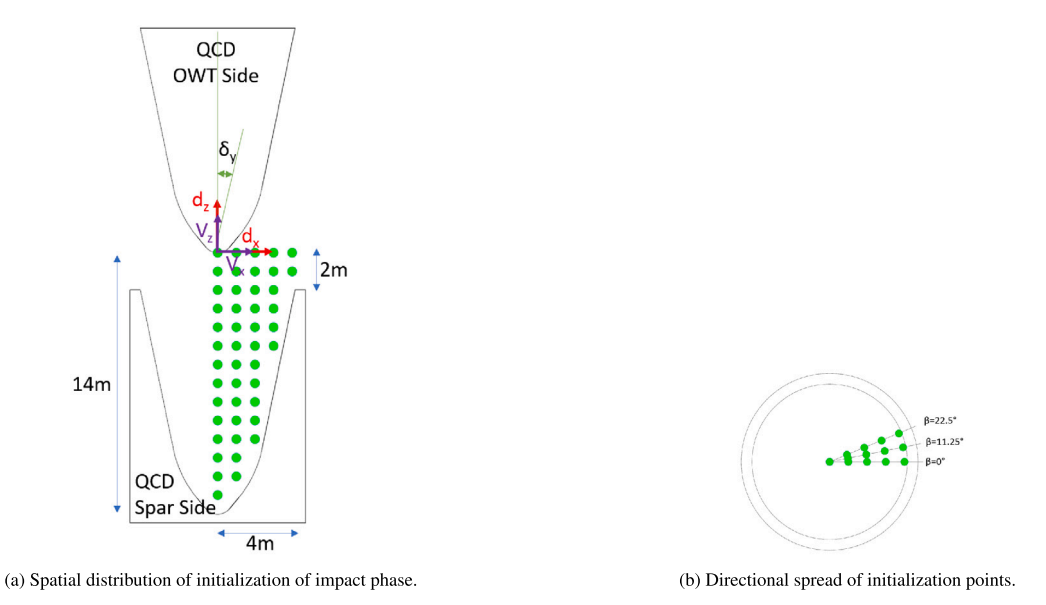


Fig. 9. Spatial distribution of possible impact scenarios.

3.5. Explicit dynamic analysis

The explicit dynamic procedure is utilized to solve the equations of the motions in the finite element simulations. The approach is appropriate as it does not require performing iterations and calculations of tangent stiffness matrices, and it simplifies the contact implementation. The equation of motions is defined as:

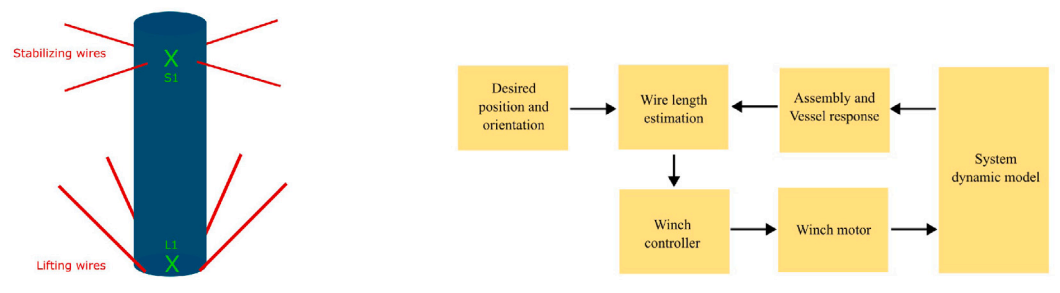
$$\ddot{u}_{(i)}^{N} = \left(M^{NJ}\right)^{-1} \left(P_{(i)}^{J} - I_{(i)}^{J}\right) \tag{1}$$

where $\ddot{\mathbf{u}}$ is the acceleration vector, M^{NJ} is the mass matrix, P^{j} is the external force vector, and I^{J} is the internal force vector. The central difference numerical approach is used as the integration rule for solving the equations of motion. In this approach, the simulation time is advanced in half steps until the whole duration is covered. This method is defined by:

$$\dot{u}^{(i+\frac{1}{2})} = \dot{u}^{(i-\frac{1}{2})} + \frac{\Delta t^{(i+1)} + \Delta^{(i)}}{2} \ddot{u}^{(i)} \tag{2}$$

$$u^{(i+1)} = u^{(i)} + \Delta t^{(i+1)} \dot{u}^{(i+\frac{1}{2})}$$
(3)

where u and \dot{u} are displacement and velocity vectors, respectively. In the explicit dynamic simulations, the time step (Δt) must be carefully selected to ensure the dynamic explicit algorithm satisfies the stability condition and reaches accurate results. This is



(a) Lifting and stabilizing wire arrangement and corresponding reference nodes

(b) Overview of the control system methodology

Fig. 10. Active control system of the lifted OWT.

ensured by the time step $\Delta t \leq \frac{2}{\omega_{max}}$, where ω_{max} is the highest natural frequency. The minimum time step can be conservatively approximated by $\Delta t \approx \frac{L_e}{C_d}$ where L_e is the minimum element length and C_d is the wave propagation speed of the material.

The contact behavior is assessed by dividing the contact region into master and slave regions, where the nodes on the slave region were not allowed to penetrate into the master region. In the case of contact, the forces are assessed in normal and tangential directions. The normal behavior is modeled by assuming a "hard" contact pressure-overclosure method, while tangential behavior is implemented using the penalty friction formulation.

3.6. Active control of the lifted assembly

One of the measures that can reduce the impact damage is to implement an active or passive control system to reduce the motions of the moving objects. An active control system is designed as it is better suited to operate in a broader range of environmental conditions and installation scenarios.

In earlier research [15], an active control system was developed to control the lifted assembly using a multi-wire arrangement. In this research, it was shown that the position of a point in 3D space, such as S1 in Fig. 10(a), can be estimated by calculating the distance of this node to four other points with known coordinates. The coordination of node S1 can be calculated by stabilizing wire lengths and the coordination of the wire connection nodes. The same applies to the lifting wires. The lifted OWT's translation and rotation can be reduced by controlling the coordination of nodes S1 and S2 in the space.

Fig. 10(b) shows an overview of the control system methodology. The desired position and orientation of the OWT are calculated in every time step of the analysis; accordingly, the suitable wire length is calculated for every single wire. The wire length is given as input to the winch controller, which provides the correct command for the winch. This information will be utilized in the system dynamics model, where the new state of the vessel and assembly is calculated. The process is followed for the whole duration of the simulation. The details of this control system can be found in the mentioned article [15].

4. Results and discussions

4.1. Relative velocities

This paper aims to describe the mating between the spar and OWT and design a suitable connection device as the crucial component. Multiple criteria must be considered to develop a successful quick connection device, such as the optimal geometry of the connection, impact forces, and long-term performance. The main focus of this article is the impact phase of the mating operation, and the impact velocity is the primary input for this analysis. The global model is used to calculate the impact velocities by exciting the floating bodies with waves. Furthermore, the responses of the different objects are reported in the time domain.

A snapshot of time histories of relative velocities between OWT bottom and spar top for $H_s=1$ m and $T_p=10$ s with the duration of 100 s is presented in Fig. 11. The red dots in sub-figures show the maximum values in each response. The maximum values of these responses do not happen simultaneously, meaning that selecting all the maximum values of the relative responses for the impact analysis might be an over-conservative assumption. However, the co-occurrence of the peaks needs to be investigated within the entire duration of the simulations and all different environmental conditions.

The summary of absolute maximum values of relative horizontal and vertical velocities and relative alignment angles for different peak periods are presented in Fig. 12. The maximum relative horizontal velocity in X-direction V_x =1.77 m/s takes place at T_p = 14 s where spar buoy pitch natural period is located (see Fig. 12(a)). The maximum vertical velocity in Z-direction V_z =2.92 m/s and maximum relative angle around the *Y*-axis R_y =5.13 deg take place at T_p = 12 s, which is in line with the catamaran vessels pitch natural period (see Figs. 12(b-c)).

All the environmental conditions were investigated individually, and the coincidence of the maximum values was studied. The summary of maximum relative velocities and relative alignments is presented in Table 2. The environmental conditions (H_s and T_p), maximum values of the responses (V_x , V_z and R_v), the time the peaks take place (Time), standard deviation (STD) of the maximum

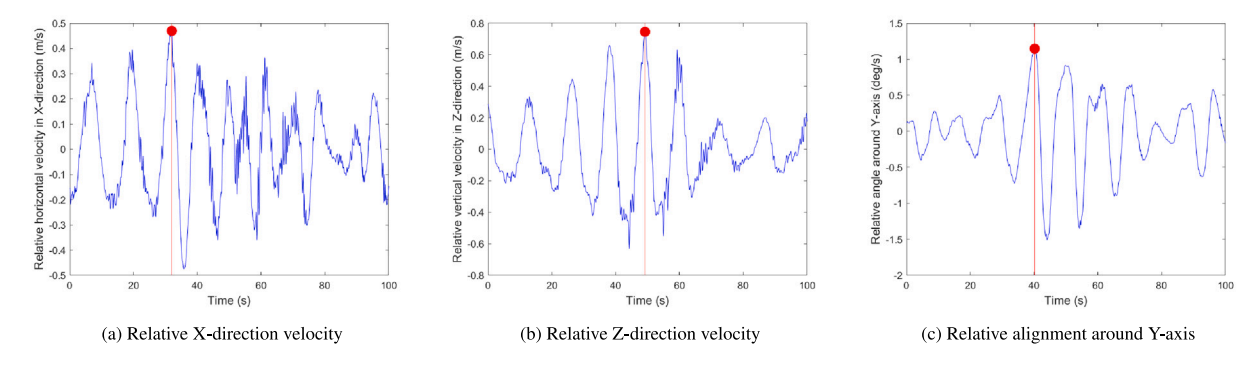


Fig. 11. Time histories of relative velocity in X- and Z-directions and relative alignment around Y-axis for $H_s = 1$ m and $T_n = 10$ s with the duration of 100 s.

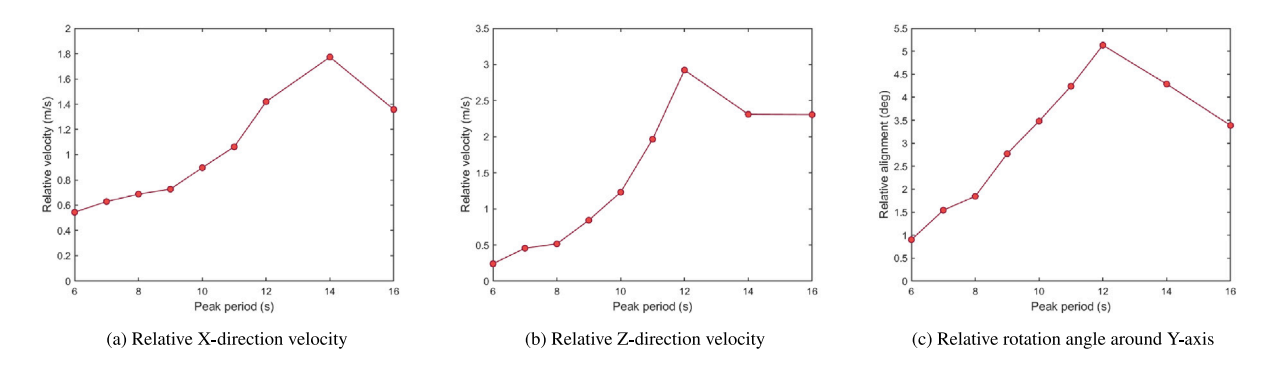


Fig. 12. Summary of absolute maximum relative motions between OWT bottom and spar top.

Table 2
Summary of absolute maximum relative velocities and relative alignment angles in different environmental conditions

conditions.								
Hs	Tp	Time (s)	V_x (m/s)	V_z (m/s)	R_y (deg)	STD		
1	14	420.3	1.77	1.28	0.96	0.453		
1	12	3356.8	1.05	2.92	0.44	0.678		
1	12	1579.4	0.23	0.39	5.13	1.463		

response and corresponding other relative responses are shown here. The bold values are the absolute maximums that occur in the simulated sea state and its STD. It is observed that the maximum values on each response do not happen simultaneously; therefore, selecting the maximum values as the impact analysis inputs is a conservative assumption. Fitting the data to the Rayleigh distribution is a good approximation for the probability density of the maxima [29]. The selected maximum absolute values result in 99% confidence concerning the Rayleigh probability density function.

4.2. Local FE results

The details of Local FE results are given in the upcoming section.

4.3. Mesh sensitivity study

Mesh sensitivity is performed to calculate the appropriate mesh size. This study helps to ensure that the finite element model can provide accurate results while maintaining the computational expenses at an optimum level. The shell elements' dimensions are selected to be 200 mm, 150 mm, 100 mm, 50 mm, and 25 mm. The maximum Von Mises stress, stable time increment, and number of shell elements are reported in Fig. 13. These results are presented for a case study with impact velocities of $V_z = -1.28$ m/s and $V_x = 1.77$ m/s.

The maximum Von Mises stress for the model with an element size of 200 mm is 595 MPa (see Fig. 13(a)). Mesh refinement to 150 mm increases the Maximum Von Mises stress to 652 MPa. Further mesh refinement to 100 mm, 50 mm, and 25 mm results in 662 MPa, 655 MPa, and 650 MPa stresses, which are very close. This is more significant for the meshes of 25 mm and 50 mm. Fig. 13(b) illustrates the absolute difference of maximum stress values between two consecutive element sizes in percentage. As the Figure shows, the difference for the last three element sizes reaches 1.8%, 1.2%, and 0.7%, which are in close proximity.

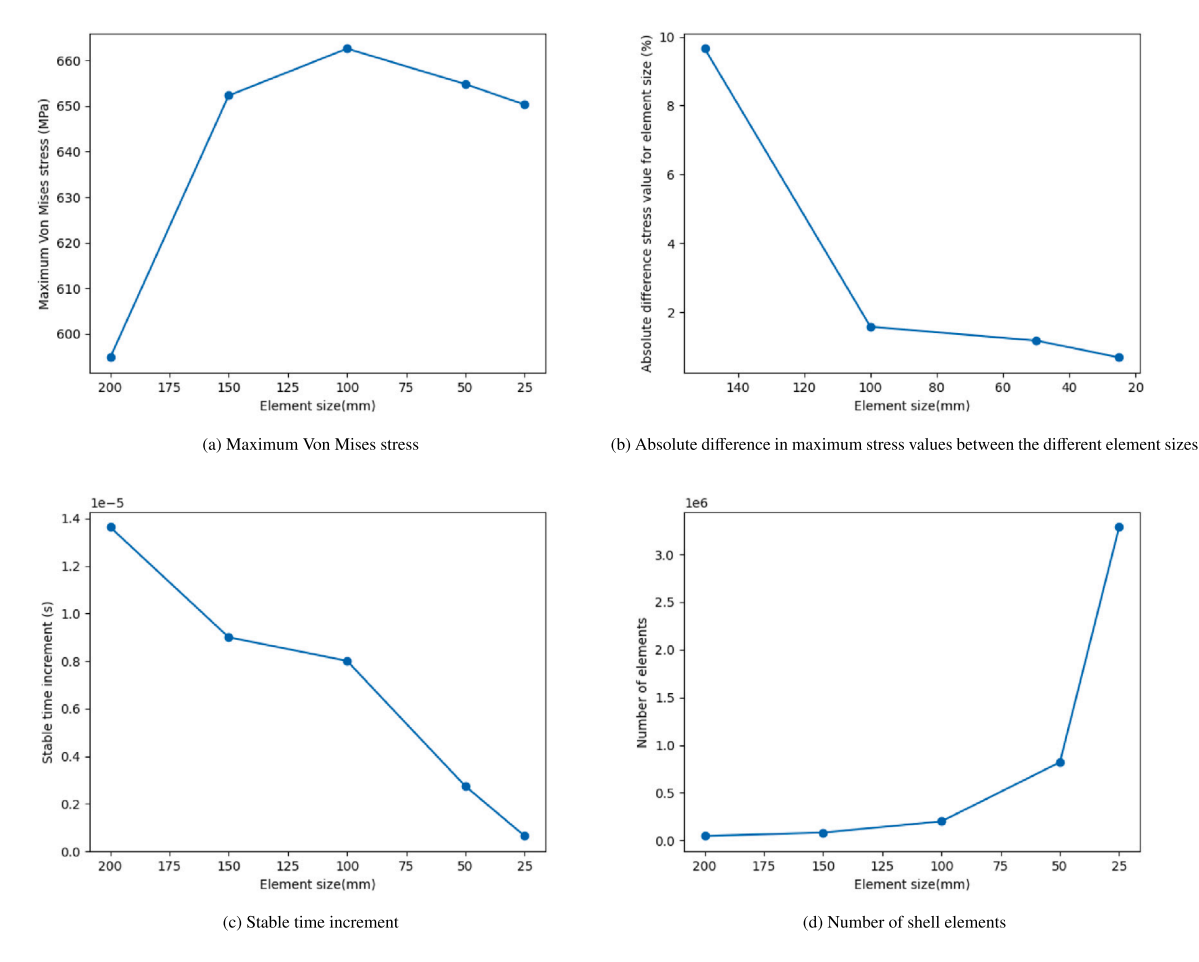


Fig. 13. Results of mesh sensitivity analysis.

The deformed shape of the impact region right after the impact is presented in Fig. 14. In the sub Figs. 14(a–(c)), the initiations of the impact regions are highlighted with red arrows, and the contours show the Von Mises stresses. All three meshes can address the overall stress behavior in the impact region. However, when it comes to deformations in this area, the model with mesh sizes of 100 mm (Fig. 14(c) is unable to capture the deformation pattern in this region fully. In two models with mesh sizes of 50 mm and 25 mm (Figs. 14(a and (b)) the deformation shapes are very similar to each other.

Mesh refinement increases the number of elements and reduces the stable time increment (see Figs. 13(c-(d)). These two phenomena increase the computation costs of the simulations. To keep the computational costs at a reasonable level and maintain modeling accuracy, the mesh size is selected as 50 mm. This selection also keeps the ratio of element size to plate thickness ≈ 1 (plates have 38 mm thickness). The analysis is performed on a workstation with an Intel Xeon 3.2 GHz CPU and 32 GB of RAM. One run for the model with a mesh element size of 50 mm took 25619 s to perform.

The stable time step of the explicit solver depends on the minimum length of elements and the wave velocity in the material. The wave speed in a material property is calculated based on the Young modulus and the material density. Based on the mesh element dimensions and the steel properties, the stable time increments in Fig. 13(a) are selected. However, the elements deform during the impact, so the minimum element length might change. Therefore, the value of stable time increment needs to be observed and modified as the simulation progresses. This research allowed the solver to select the explicit time step automatically.

The energy output history of the system indicates the simulation validity, when explicit solvers are utilized. The system's energy balance levels during the simulation with a duration of 2 s and $V_x=1.77\,$ m/s and $V_z=-1.28\,$ m/s are presented in Fig. 15. The total energy (ETOTAL) stays at a constant level equal to the analytical kinetic energy at the beginning of the impact. The impact between the bodies initiates around 0.85 s and ends around 1.25 s. Total kinetic energy (ALLKE) remains equal to the ETOTAL until the initialization of impact, where it converts to other energies. Part of the total energy is absorbed as frictional dissipation and plastic deformation. During the impact phase, some kinetic energy is absorbed as strain energy (ALLSE) by elastic deformation, which is released when the impact is complete.

Artificial energy (ALLAE) is the amount of energy added to the system to keep the energy balance and address the hourglassing of the shell elements. The ratio of artificial energy (ALLAE) to internal energy (ALLIE) energy should be kept below 5% [33]. The maximum ratio of ALLAE/ALLIE is 2.8%, which is less than the recommended value.

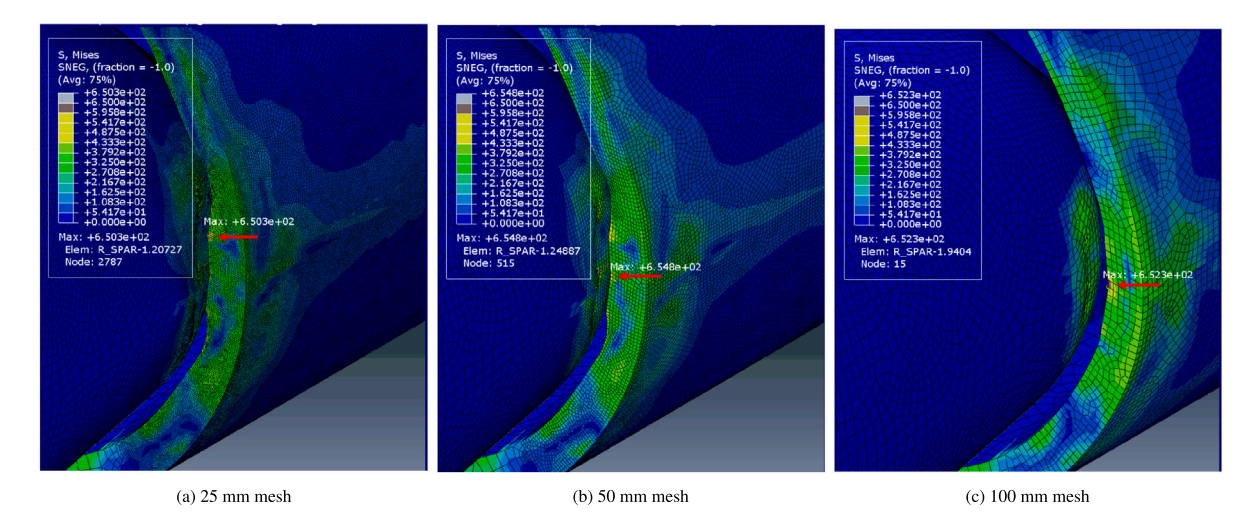


Fig. 14. Results of mesh sensitivity analysis for the element sizes of 25 mm, 50 mm, and 100 mm.

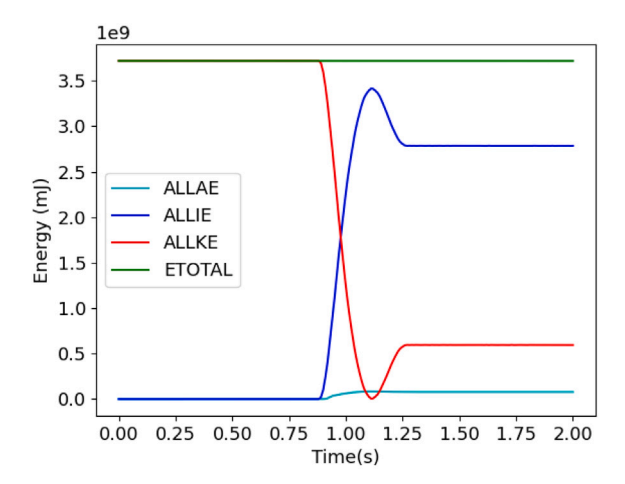


Fig. 15. Energy distribution during the impact.

Measures can be taken to reduce the severity of the impact during the mating operation. The first is to implement the substructure's hydrostatic stiffness, and the second is to passively or actively control the lifted assembly.

In the mesh sensitivity analysis, the spar is assumed to be fixed, which is a conservative assumption. However, in reality, the spar can move within the boundaries enforced by mooring lines. Implementing the hydrostatic stiffness of the spar in the finite element model is expected to reduce the impact damage and improve the simulation fidelity. Furthermore, active control of the hanging OWT can reduce the relative velocities and alignment between the two bodies (OWT and spar), resulting in a softer impact.

4.4. Effect of hydrostatic stiffness

Generally, the impact is a very abrupt phenomenon that takes place within a portion of a second. However, in the SFI-Move installation concept, the velocities and accelerations are relatively low due to large masses of objects and high inertial forces. This allows the spar foundation hydrostatic stiffness activation during the impact phase. The updated model takes into account the hydrostatic stiffness and the stiffness from the mooring lines, which reduces both impact deformation and, consequently, energy absorption. The low hydrostatic stiffness of the spar, especially in horizontal directions (surge and sway), strengthens the influence.

The needed stiffness in each case can be implemented using transitional and rotational springs in the FE model (see Fig. 16).

The hydrostatic stiffness of the spar is composed of contributions from the water plane area and mooring lines. The first term depends on the geometry of the floating body and mass distribution, estimated during stability analysis. The mooring lines' contribution to the hydrostatic stiffness is estimated by inserting the horizontal forces at the top of the spar (Z = 20 m). The translation and the rotation at its COG are measured. Due to the arrangement of the mooring lines, impact direction is expected to vary the stiffness of the springs. Five load cases (LCs) are defined to estimate the stiffness variation by the impact direction (see

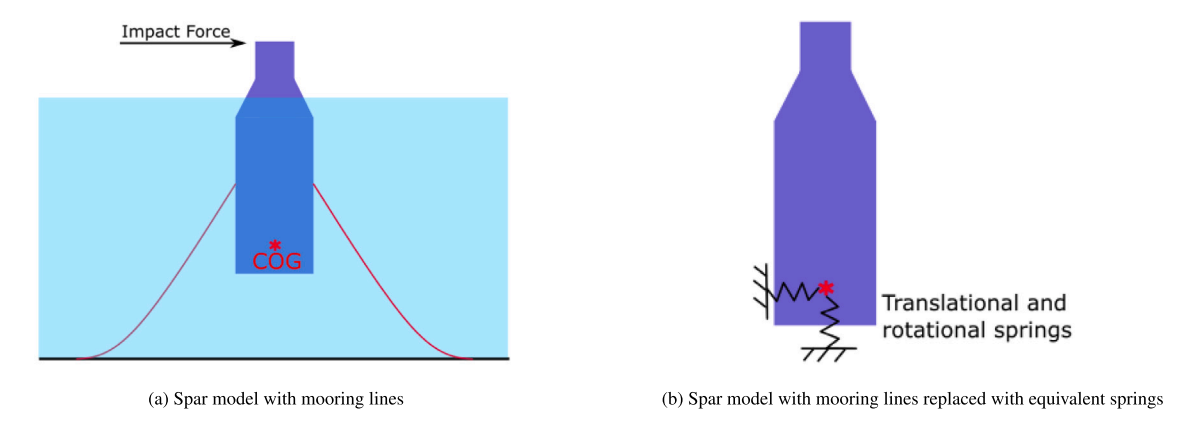


Fig. 16. Spar foundation hydrostatic stiffness replication with translational and rotational springs.

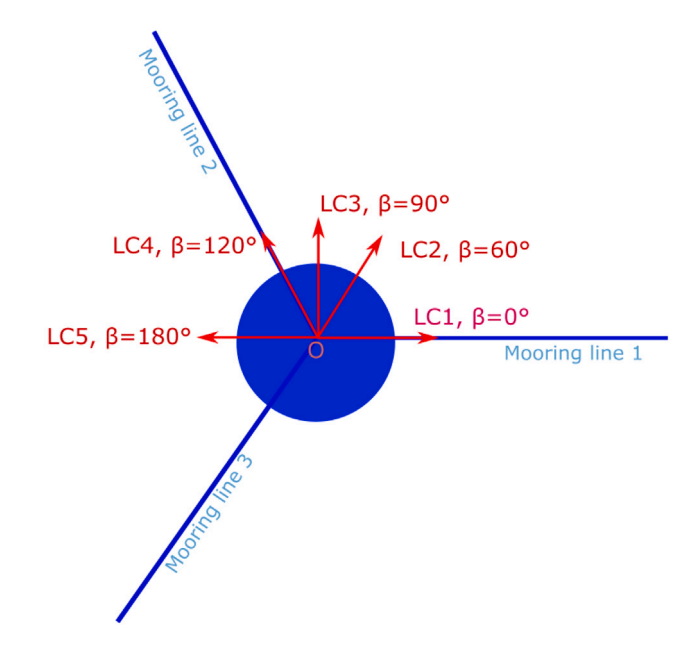


Fig. 17. Orientation of load cases for the estimation of mooring lines' contribution to the hydrostatic stiffness.

Fig. 17). These five load cases are selected within the $0 \le \beta \le 180^{\circ}$, as the spar and mooring lines have symmetry around the horizontal axis.

The force-displacement and force-rotation of the spar COG for different LCs are presented in Fig. 18.

Both translation and rotation of the spar COG have behavior that is nearly linear according to Figs. 18(a–b). Therefore, implementing mooring lines with linear springs is a realistic assumption. Fig. 18(a) shows that LC1 and LC4 have identical behaviors as both take place in the direction of one of the mooring lines. In addition, these two LCs provide the highest stiffness, as two mooring lines contribute to the reaction in the direction of the force. LC2 and LC4 have an identical response with the least stiffness, as only one mooring line contributes to these LCs. The LC3's force-transition result falls in between the results of the other LCs. The rotation of the spar COG is identical between all the LCs, as the mooring connection lines and the impact force elevations are at the same height, which provides similar rotational stiffness between all these LCs.

The softer spring is expected to allow higher energy absorption levels during the impact. Therefore, the stiffest cases (LC2 and LC5) are selected for the contribution of the mooring lines to the spar hydrostatic stiffness. This results in selecting the most conservative LC for mooring line stiffness implementation. The spar transitional stiffness in the global X- and Y-directions is only rooted in the contribution of mooring lines. Furthermore, for the roll and pitch DOFs, the contribution of the mooring lines must be added to the part produced by the water plane area. The contributions of the mooring lines' stiffness to the hydrostatic stiffness in the direction of the impact are summarized in Table 3.

The equivalent hydrostatic springs are added to the finite element model. Decay tests are performed to ensure identical behavior between the finite element model and the hydrodynamic model. These tests are done in surge, heave, and pitch degrees of freedom,

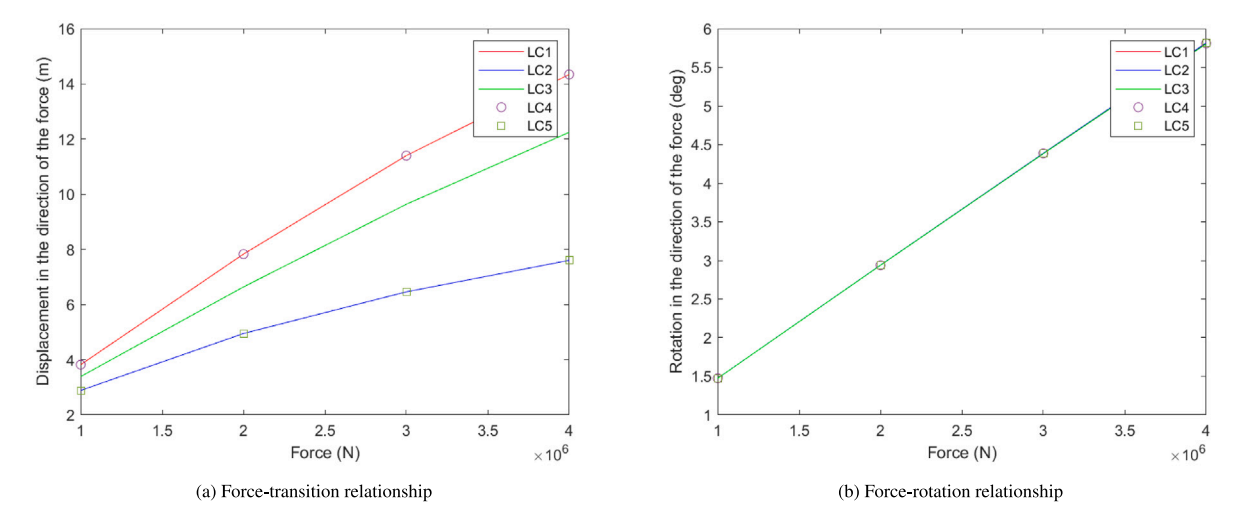


Fig. 18. Spar COG translation and rotation.

 Table 3

 Summary of hydrostatic stiffness contribution from the mooring lines (stiffness values are provided in the direction of the impact).

Load case	Longitudinal	Rotational		
	Stiffness	Stiffness		
	(N/m)	(Nm/Deg)		
LC 1	2.65E+05	4.82E+07		
LC 2	4.35E+05	4.82E+07		
LC 3	3.08E+05	4.82E+07		
LC 4	2.65E+05	4.82E+07		
LC 5	4.35E+05	4.82E+07		

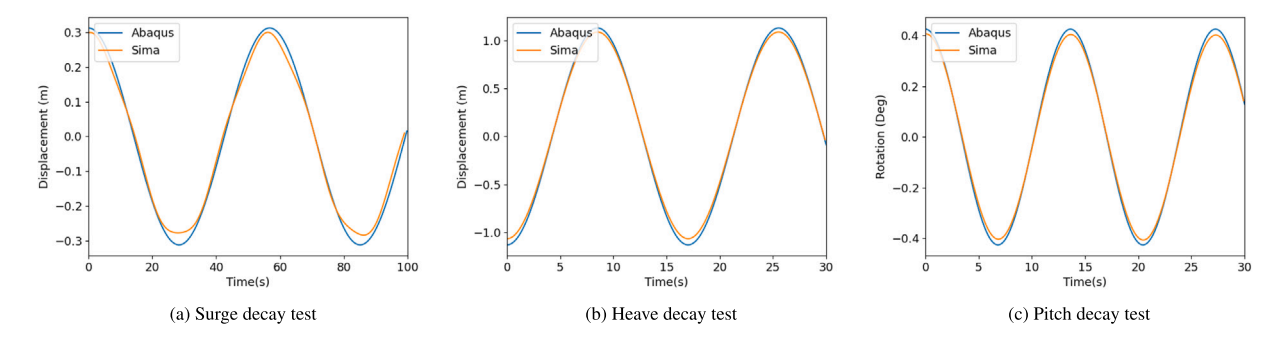


Fig. 19. Decay tests in heave and pitch degree of freedoms.

where an initial force (for surge and heave) and moment (for pitch) are inserted into the model. The structure is allowed to reach the static equilibrium under these excitations and then released to enable the system to vibrate freely. In Fig. 19, the decay test results of the spar buoy modeled in Abaqus and Sima are presented.

In all three DOFs, the models have behaviors that are close to each other. The static equilibrium is comparable in all three cases, and the free vibrations are very close in all tests. A minor peak amplitude difference in tests is seen where the Sima model has slightly lower values. This difference is more significant in the surge; see Fig. 19(a). The models are vibrating with spar moored surge natural frequency of T_{11} = 56.7s, heave natural period of T_{33} = 17 s, and pitch natural period T_{55} = 13.7s.

The impact energy balance with and without considering the hydrostatic stiffness is presented in Fig. 20. In both models, the total energy is equal to the initial total kinetic energy, which comes from the motion of the OWT. However, as the impact initiates, the two models have different behaviors. In the model with hydrostatic stiffness, as the impact initiates, the spar foundation starts to move. This results in the conversion of less total energy to the internal energy as shown in Fig. 20(a). The contribution of plastic dissipation to the internal energy is presented in the 20(b). It can be seen that the plastic dissipation contribution to the internal energy is a lot higher in the fixed model, meaning that plastic deformation is more significant.

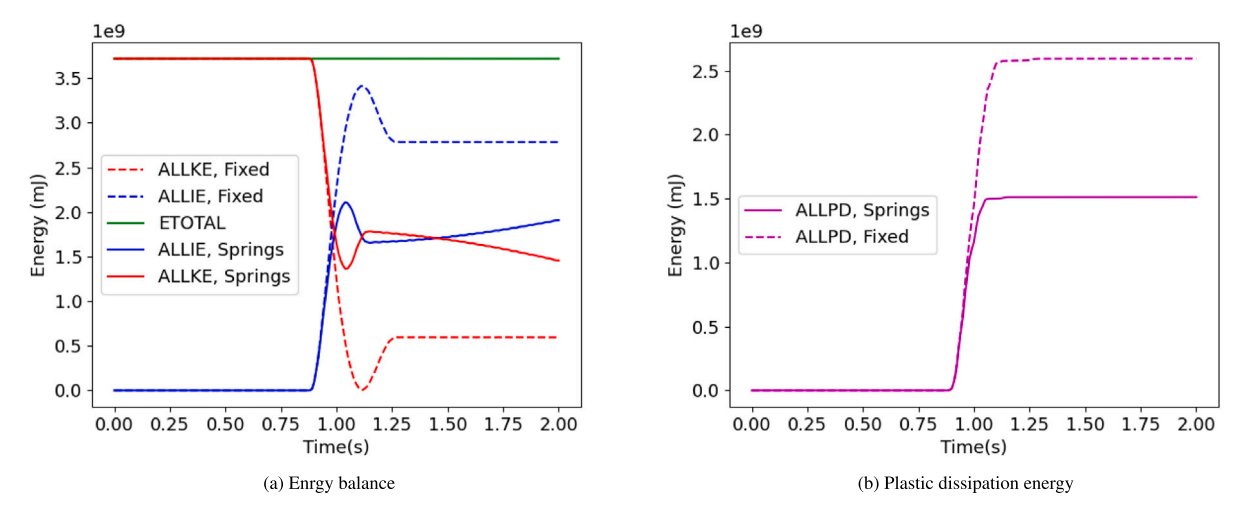


Fig. 20. Energy comparison between fixed model and model with hydrostatic stiffness.

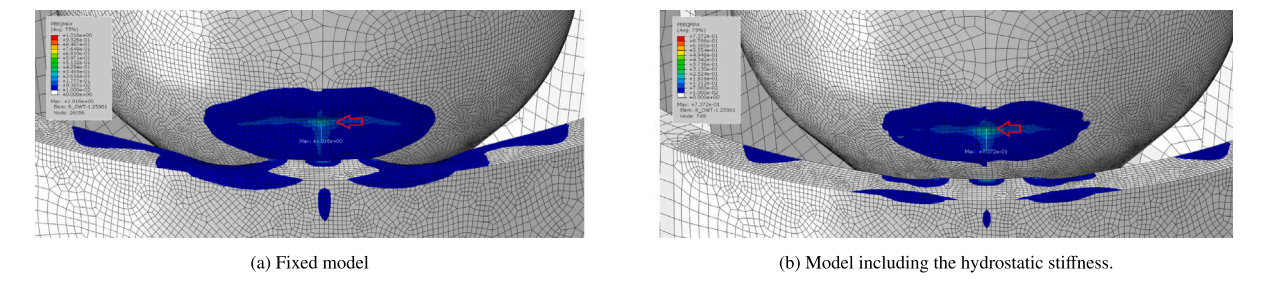


Fig. 21. Comparison of equivalent plastic strain between the fixed model and the model with hydrostatic springs.

The equivalent plastic strain (PEEQ) [34] is a scalar variable to quantify the inelastic deformations. Equivalent plastic strain is calculated by integrating the equivalent plastic strain rate over the time deformation history. The comparison of the PEEQ for the models with and without the hydrostatic stiffness is given in Fig. 21.

In Fig. 21, the values and spread of plastic deformations are larger in the fixed model. The model with the hydrostatic springs absorbed some of the impact energy via elastic deformations of the springs. As a result, softer impacts took place. We conclude that the model with hydrostatic springs is a better representation of reality in addition to exhibiting more desirable behavior from the impact perspective. Therefore, this model will be utilized to assess the impact scenarios in this research.

4.5. Impact scenarios

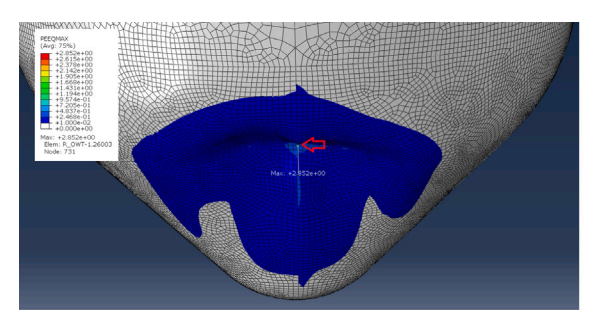
The different impact scenarios are simulated according to the geometrical distribution of impact initiation points in Fig. 9. The tip of the OWT is located on the green dots in different impact scenarios. The relative horizontal and vertical distance between OWT and spar are considered by inserting the OWT tip in these locations. The relative alignment is implemented by rotating the OWT, and the spar is assumed to be upright. The total relative velocities are inserted into the OWT, and the spar's initial velocity is set to zero. The simulation is initiated by inserting the initial velocity into the OWT, which continues until the impact ends.

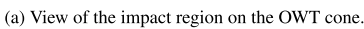
The relative distance between the QCD at OWT and spar sides (d_x and d_z), relative velocity (V_x and V_z), relative alignment (δ_y), and misalignment (β) are used as variables to define the different impact cases. The input parameters are illustrated in Fig. 9. The results of different impact scenarios are summarized in Table 4. The maximum Von Mises stress and PEEQ and their corresponding locations are reported as results. The reported results are the maximum values throughout the simulation duration.

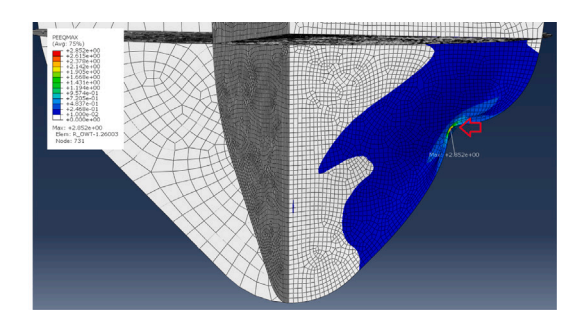
The plastic deformations happen on both sides of the quick connection device, and the spar and OWT tubes are not damaged for the cases with $\beta < 22.5^{\circ}$. Therefore, the quick connection device can isolate the impact region from the OWT and spar main structures by restricting the operation to the following sea waves. Most of the maximum plastic deformations occurred on the QCD OWT stiffeners and spar top plate. The maximum plastic deformation happens for LC 0-02-1 with a value of PEEQ=2.85, which takes place on the OWT side of the QCD at stiffener plates; see Fig. 22. These plates are prone to lateral buckling when impact happens in their plane. The maximum stress occurs at LC 0-01-0, with a value of 872.4 MPa at the spar impact plates' location; see Fig. 23. The Von Mises stresses are calculated at the integration points and extrapolated to the shell elements' edges. That is why the stress values in the element corners are higher than the yield defined in the bilinear stress–strain curve defined in Fig. 8.

Table 4
Summary of finite element model results.

Load case	dx (mm)	dz (mm)	Vx (m/s)	Vz (m/s)	δ_x (deg)	β (deg)	Max. Stress (MPa)	Location	Max. PEEQ	Location
LC 0-01-0	0	0	1770	-2920	0.00	0.00	872.4	Spar Impact Plates	2.772	OWT Stiffener
LC 0-01-1	0	0	1770	-2920	5.13	0.00	627.1	OWT Stiffener	0.198	OWT Stiffener
LC 0-01-2	0	0	1770	-2920	-5.13	0.00	664.7	Spar Stiffener	1.270	OWT Stiffener
LC 0-02-0	1000	0	1770	-2920	0.00	0.00	782.4	OWT Cone	1.776	OWT Stiffener
LC 0-02-1	1000	0	1770	-2920	5.13	0.00	784.2	Spar Impact Plates	2.852	OWT Stiffener
LC 0-02-2	1000	0	1770	-2920	-5.13	0.00	744.2	Spar Impact Plates	2.505	OWT Stiffener
LC 0-03-0	2000	0	1770	-2920	0.00	0.00	632.2	OWT Stiffener	2.502	OWT Stiffener
LC 0-03-1	2000	0	1770	-2920	5.13	0.00	742.0	OWT Cone	2.592	OWT Stiffener
LC 0-03-2	2000	0	1770	-2920	-5.13	0.00	692.0	Spar Stiffener	1.393	Spar Stiffener
LC 0-10-0	0	-1000	1770	-2920	0.00	0.00	630.0	OWT Stiffener	2.300	OWT Stiffener
LC 0-10-1	0	-1000	1770	-2920	5.13	0.00	666.3	Spar Top Plate	0.251	Spar Top Plate
LC 0-10-2	0	-1000	1770	-2920	-5.13	0.00	636.0	Spar Impact Plates	2.349	OWT Stiffener
LC 0-20-0	0	-2000	1770	-2920	0.00	0.00	657.2	OWT Stiffener	0.540	OWT Stiffener
LC 0-20-1	0	-2000	1770	-2920	5.13	0.00	660.5	Spar Top Plate	0.249	Spar Top Plate
LC 0-20-2	0	-2000	1770	-2920	-5.13	0.00	658.2	Spar Impact Plates	2.571	OWT Stiffener
LC 0-50-0	0	-5000	1770	-2920	0.00	0.00	496.7	Spar Outer Tube	0.137	Spar Top Plate
LC 0-50-1	0	-5000	1770	-2920	5.13	0.00	744.2	Spar Top Plate	0.224	Spar Top Plate
LC 0-50-2	0	-5000	1770	-2920	-5.13	0.00	573.0	Spar Stiffener	0.509	Spar Stiffener
LC0-22-0	2000	-2000	1770	-2920	0.00	0.00	747.6	OWT Cone	2.351	OWT Stiffener
LC0-22-1	2000	-2000	1770	-2920	5.13	0.00	678.1	OWT Cone	2.456	OWT Stiffener
LC0-22-2	2000	-2000	1770	-2920	-5.13	0.00	646.4	Spar Impact Plates	2.329	OWT Stiffener
LC 1-02-0	0	-2000	1770	-2920	0.00	11.25	669.1	Spar Impact Plates	0.769	Spar Top Plate
LC 1-02-1	0	-2000	1770	-2920	5.13	11.25	577.4	Spar Top Plate	0.528	Spar Top Plate
LC 1-02-2	0	-2000	1770	-2920	-5.13	11.25	630.4	OWT Cone	0.899	Spar Impact Plates
LC 2-01-0	0	0	1770	-2920	0.00	22.50	549.0	Spar Impact Plates	0.232	Spar Impact Plates
LC 2-01-1	0	0	1770	-2920	5.13	22.50	769.0	Spar Outer Tube	0.653	Spar Top Plate
LC 2-01-2	0	0	1770	-2920	-5.13	22.50	776.8	Spar Outer Tube	0.512	Spar Top plate
LC 2-22-0	2000	-2000	1770	-2920	0.00	22.50	812.5	Spar Outer Tube	0.598	Spar Top Plate
LC 2-22-1	2000	-2000	1770	-2920	5.13	22.50	648.7	Spar Outer Tube	0.582	Spar Top Plate
LC 2-22-2	2000	-2000	1770	-2920	-5.13	22.50	792.5	Spar Outer Tube	0.960	Spar Top Plate







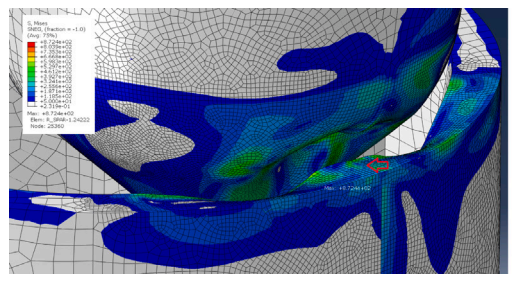
(b) Out of place buckling of OWT stiffener plate.

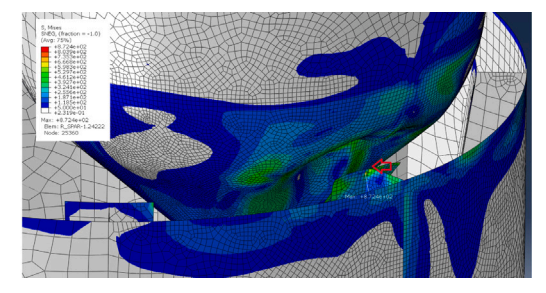
Fig. 22. Maximum PEEQ for LC 0-02-1 at OWT stiffener.

The approach of OWT to the spar initiates when the vertical distance between the OWT and spar is 2 m. For the mating operation to occur successfully, the horizontal distance between the OWT QCD tip, the spar QCD center, and the entrance velocity becomes critical. Fig. 24 illustrates three load conditions where Δ_x =-2000 mm and δ_y is varied. At a horizontal distance of 3 m with the maximum relative velocities, the mating becomes unsuccessful for the relative angle of δ_x =-5.13 deg (LC 0-03-2). At the horizontal distance of 4 m, the mating becomes unsuccessful independent of the relative alignment. Therefore, limiting the horizontal distance to less than 3 m is recommended.

The impact scenarios are more severe when the impact initiates at higher vertical distances between QCD at both ends (cases where dz=0 mm such as LC 0-01-0). A comparison of Von Mises stresses between the LC 0-01-0 and LC 0-50-0 with vertical displacement of -5 m is presented in Fig. 25. The greater severity of impact at the extremes is mainly due to the impact of the conic shape of the OWT QCD with the edge of QCD on the spar side. With the reduction of vertical distance, the impact becomes less critical as the shape of the QCD at both ends follows each other. Therefore, the area of the impact regions increases, which results in better distribution of the impact forces and less severe damage (LC 0-50-0, for example).

To assess the influence of operational misalignment and spreading of the waves, the relative in-plane angle β is modified. An example of PEEQ results for LC-0-01-2 with β =0° and LC2 2-01-2 with β =22.5° are illustrated in Fig. 26. The comparison of load cases LCs 0-01-0, 0-01-1, and 0-01-2 with LCs 2-01-0, 2-01-1, and 2-01-2 shows that for the cases with β =22.5 deg, the maximum





(a) Isometric view.

(b) Isometric view, Spar top plate is removed.

Fig. 23. Maximum Von Mises stress for LC 0-01-0 at Impact Plates.

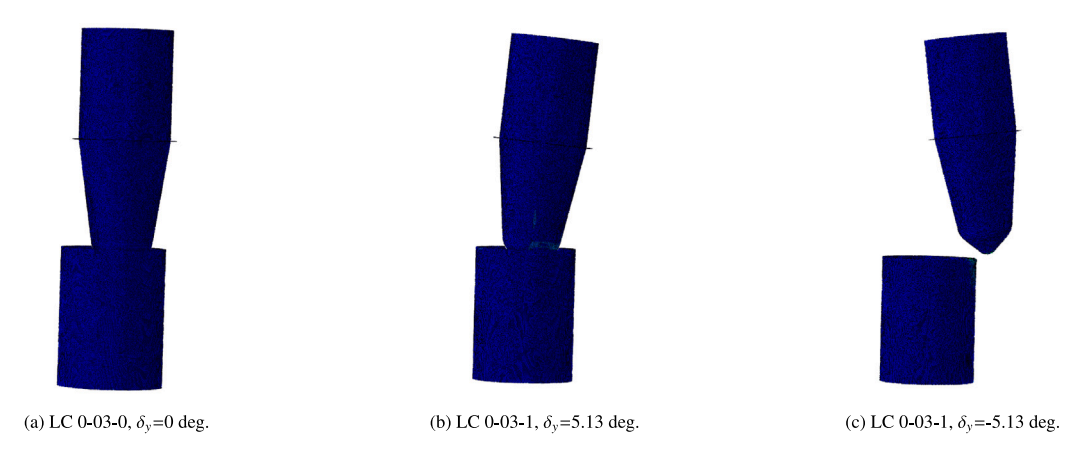


Fig. 24. Arrangement of QCD for three load cases with $\Delta_x = -2000$ mm.

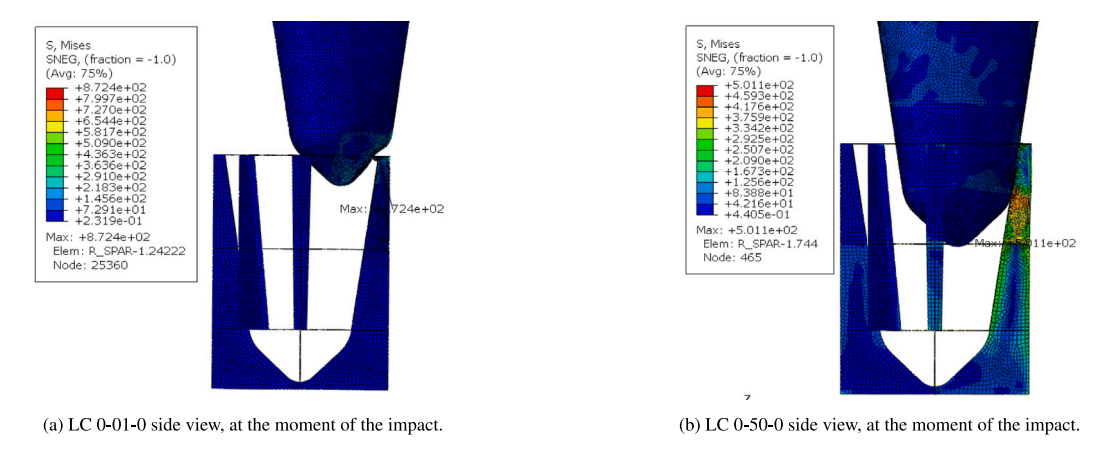


Fig. 25. Effect of penetration height on the Von Mises stress at the moment of the impact.

PEEQ is reduced; however, the nature of the impact is changed between these two scenarios. For LCs with β =0 deg, the hard impact occurs at the top of the spar stiffener plates, resulting in OWT stiffener buckling. For the cases with β =22.5 deg, the impact takes place with the edge of the spar top plates, resulting in the maximum plastic deformations in the same region. However, the tension is transferred to the spar outer tube due to the lack of stiffener under the spar top plate. This results in plastic deformation on the outer tube.

4.5.1. Desired impact configuration

Fig. 27 shows the distribution of different impact regions. It is observed that critical impacts occur with the edge of the spar at the top of QCD. The impact with the edge results in stress concentration and high plastic deformation, both of which are higher

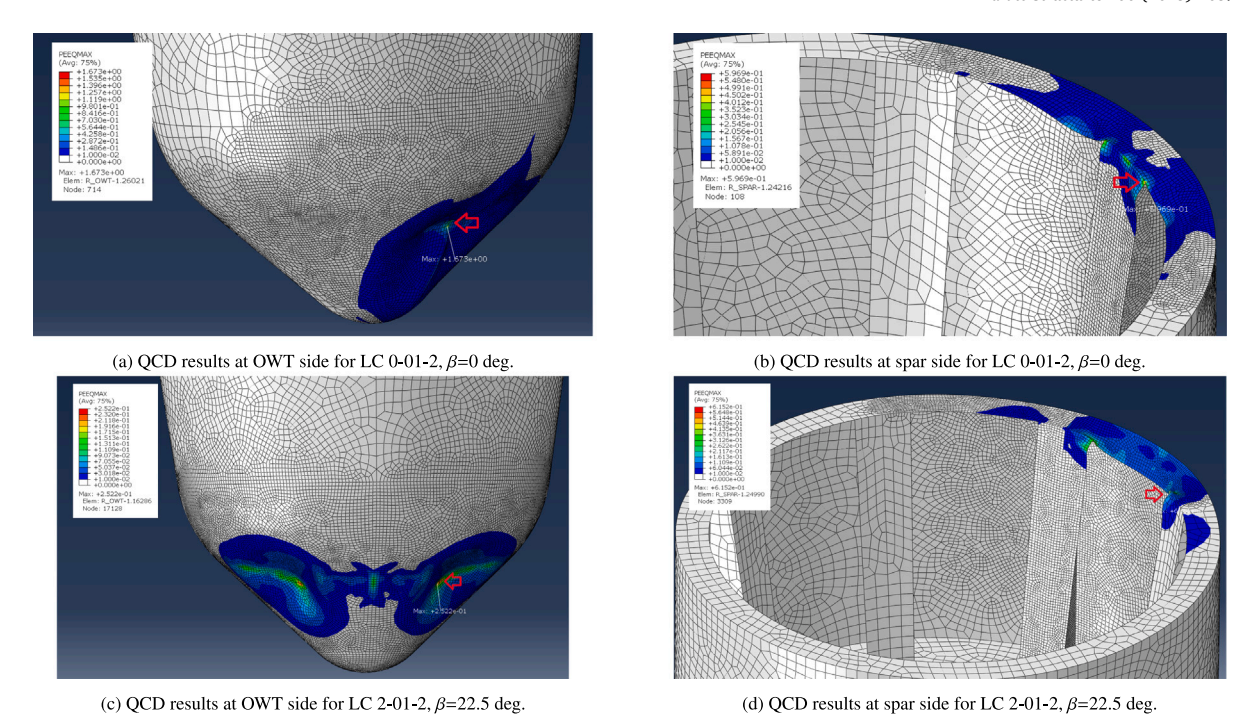


Fig. 26. Comparison of PEEQ results for two load cases with varying β .

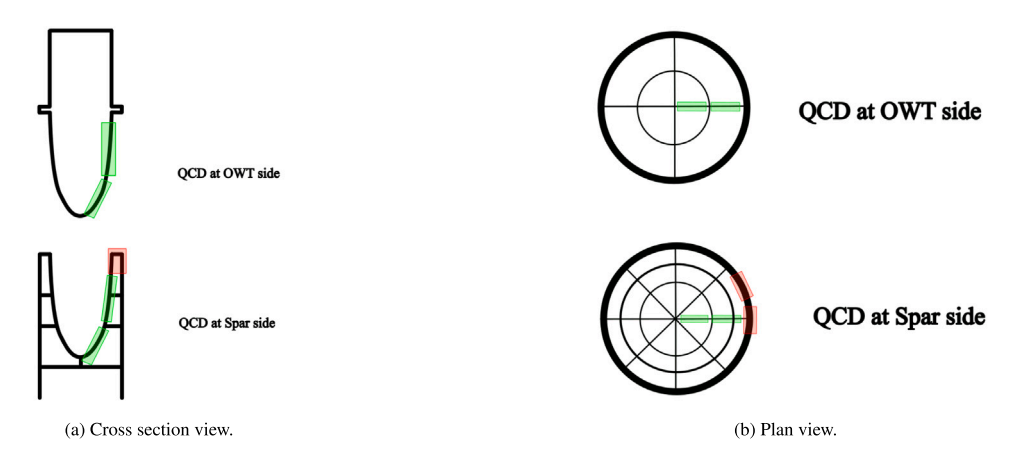


Fig. 27. Overview of critical impact locations and desired positions.

compared to other impact configurations. This critical impact region is highlighted with the red boxes in Fig. 27. The impacts with a misalignment angle higher than zero ($\beta > 0^{\circ}$) result in impact with QCD at the spar side and top plate. Because this plate does not have stiffeners in this area, it deforms vertically when impact occurs. The forces in these impact scenarios are transferred to the outer tube, resulting in plastic deformation in the outer tube in addition to the spar top plate.

The desired impact occurs when the flat regions come into contact with each other. The desired impact regions are highlighted with green colors. This is possible when enough penetration of OWT happens with larger d_z values. Furthermore, the optimal relative alignment can result in the desired impact. This is achievable with minimal relative alignment angles or optimal angles where the flat part of the QCD tip at the OWT side comes into contact with the flat region of the QCD at the spar side.

4.6. Active control of the lifted assembly

The relative velocity and alignment between the OWT and spar are the most critical inputs for the impact analysis. In an earlier study, Ren et al. [15] showed that the relative motions between the hanging OWT and a monopile were reduced using anti-swing

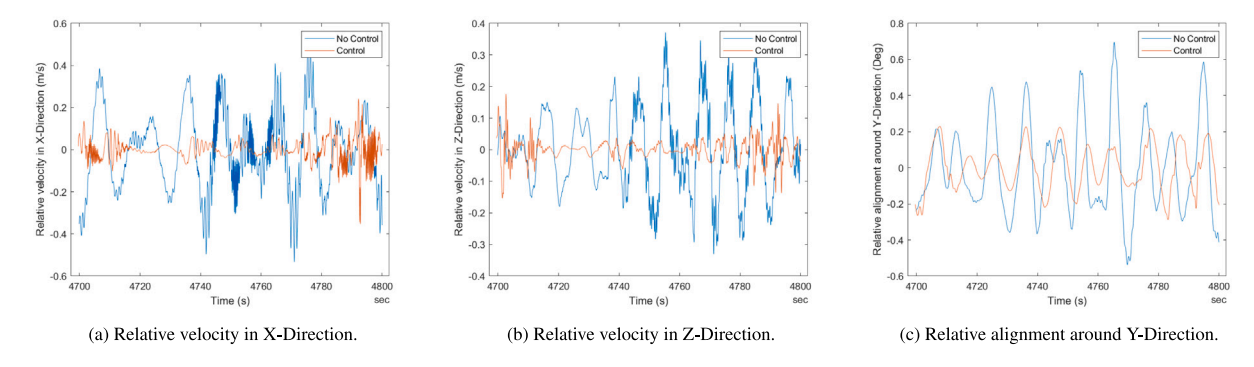


Fig. 28. Time history of relative motion between the OWT bottom and spar top with and without the presence of active control system.

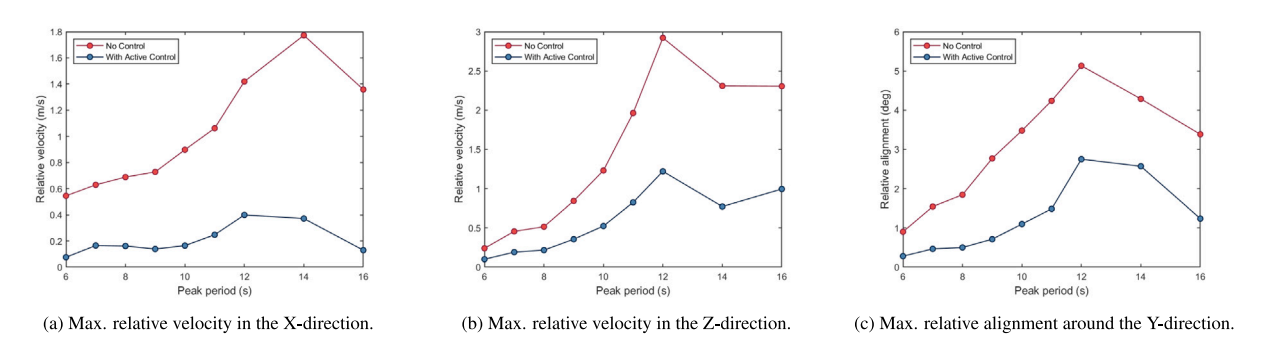


Fig. 29. Summary of maximum relative velocities for different peak periods with and without an active control system.

control. It is expected that utilizing this active control mechanism can reduce the relative velocities and alignment between the floating bodies in this study and improve the impact performance.

The simulations are performed with and without the presence of the control system. Time histories of relative motions between spar top and OWT bottom with a duration of 100 s for H_s =1 m T_p =10 s are presented in Fig. 28.

It can be seen that the active control system was able to reduce the relative horizontal and vertical velocities and relative alignment. The simulations mentioned in Section 3.1 are redone with the active control system. Fig. 29 summarizes the maximum relative velocities and alignment results with and without an active control system.

The anti-swing active control system reduced the relative velocities and alignment in all environmental conditions. This reduction is more substantial in relative velocities around the natural periods. Therefore, utilizing this control system results in a reduction in plastic deformations and improved impact performance.

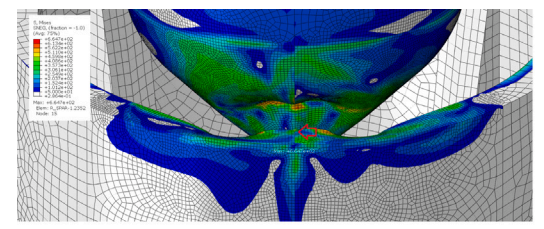
The impact scenario for LC 0-01-2 is performed with the active control system. The initial conditions for this model correspond to V_x = 0.4 m/s, V_z = -1.22 m/s and δ_y = 2.75°. The comparison of PEEQ and Von Mises stress for the two case studies is presented in Fig. 30.

Implementing the control mechanism has significantly reduced the model's Von Mises stress and PEEQ. The maximum Von Mises stress is reduced from 664.7 MPa to 616.1 MPa; see Figs. 30(a) and 30(c). The maximum PEEQ result is reduced from 1.27 to 0.50, and the spread of the deformed area is also reduced considerably; see Figs. 30(b) and 30(d).

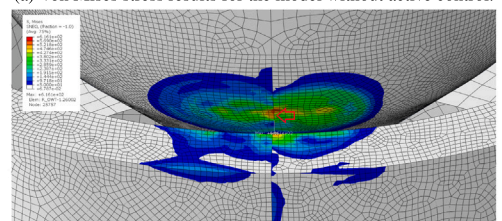
4.7. Improvement measures

One of the measures to reduce relative motions between the spar buoy and catamaran installation vessel is to install mechanical coupling between the floaters. Hong et al. [35] have proposed a winch fender system to reduce relative motions between the floating bodies. In this configuration, the winch is tensioned to a certain level to hold these bodies close to each other, and fenders are utilized to keep the offset between the floaters and dampen the relative motions. It was proved that mechanical coupling can reduce relative motions. In simulation condition 3 (SC3) of this study, the winch is pre-tensioned to 1000 KN. This level of pretension resulted in 83% and 38% reduction in relative X-direction velocity and rotation around Y-axis responses, respectively, and a 3% increase in relative Z-direction velocity for H_s =1 m.

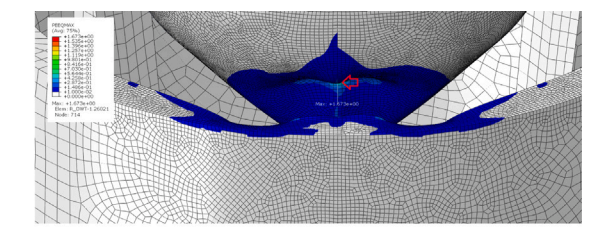
Implementing the mechanical coupling and the active control mechanism simultaneously is expected to reduce the impact damage further. Therefore, the mechanical coupling is added to the active control system simulations. Implementing mechanical coupling to the active control model resulted in maximum responses of V_x =0.36 m/s, V_z = -1.22 m/s and relative alignment of d_v =1.77°. The impact simulation is performed for the load case with d_x =0 mm and d_z =0 mm with the new inputs for relative



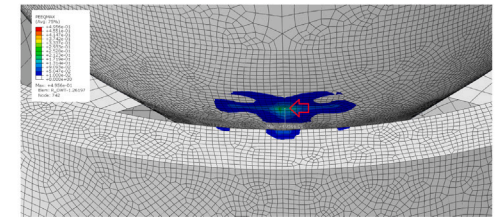
(a) Von Mises stress results for the model without active control.



(c) Von Mises stress results for the model with active control.

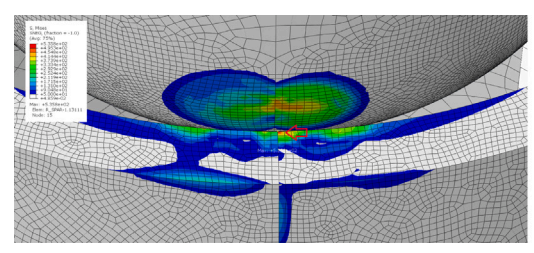


(b) PEEQ results for the model without active control.

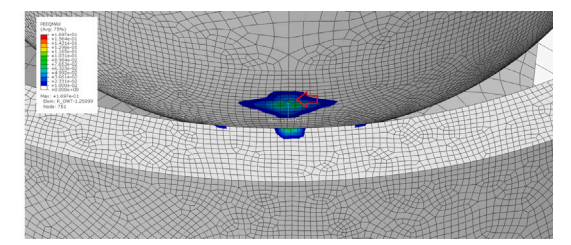


(d) PEEQ results for the model with active control.

Fig. 30. Comparison of PEEQ and Von Mises stress results for LC 0-01-2 with and without active control.



(a) Von Mises stress results.



(b) PEEQ results.

Fig. 31. Overview of analysis results including mechanical coupling and anti-swing control.

velocities and alignment. The analysis results are presented in Fig. 31. The maximum Von Mises stress is 535.8 MPa, and the maximum PEEQ is 0.17 in this case.

Implementing the mechanical coupling between the installation vessel and spar buoy while utilizing the active control has reduced relative velocities and alignment between these bodies. This resulted in the reduction of Maximum Von Mises from 667.7 MPa to 538.8 MPa and PEEQ from 0.50 to 0.17. Therefore, implementing the anti-swing control and mechanical coupling simultaneously reduces the impact damage to a minimal level.

Other measures can be taken to reduce the impact's damage during mating. The structure can be redesigned where the impacts take place, and the geometry of the quick connection can be optimized. Implementing a circular stiffener along the spar top plate edge is expected to reduce the influence of misalignment. QCD can be covered with other materials such as marine protection plates [36]. The plastic material can dampen some of the impact energy, resulting in less plastic deformation on the steel component. Using a mechanical coupling between the floating substructure and the installation vessel can influence the hydrodynamic behavior of the floating bodies. Hong et al. [35] used a fender-winch system between the catamaran vessel and the spar buoy, showing that relative motions could be reduced considerably. Solutions utilizing these measures could be studied as a continuation of the current research.

5. Conclusions and future work

One of the main issues in OWT projects is the lack of a suitable connection apparatus between the OWT and the floating substructure. The industrial designs currently in use, such as grouted and bolted connections, have limitations when installing OWTs. This article introduces an innovative concept of a quick connection device, which is expected to reduce the installation operation time. To develop an initial design of this device, a global analysis model is formulated to estimate the relative motions between the lifted OWT and the floating spar buoy. The impact forces are of significant importance, especially at the early stages of the mating operation. To assess this, a local FE model is developed to determine the impact between these bodies. Finally, anti-swing active control was utilized to reduce the relative velocities and impact damage.

In this research, the hydrostatic stiffness of the spar buoy (including the mooring lines) is calculated and implemented in the FE impact model using springs. This measure improved the simulation fidelity, increased impact energy absorption, and reduced plastic

B. Ataei et al. Marine Structures 100 (2025) 103720

deformation caused by impact. A sensitivity study of the geometrical distribution of impact initiation scenarios is performed, and it is concluded that the plastic deformation can be reduced by optimizing the location of the impact initiation point. Furthermore, the anti-swing active control system is utilized to reduce the relative motion between the hanging OWT and the floating spar buoy. This resulted in a reduction in plastic deformations of the quick connection device.

5.1. Recommendations for future research

The current research proposes an initial design for a quick connection device. The main focus here is on the impact phase of the mating operation. However, all the operation phases must be considered to perform an optimal design. This research can be extended by assessing the quick connection performance in other mating phases.

In this research, three simulation tools are utilized to address three different aspects of the problem: hydrodynamics, impact, and control systems. Each of these disciplines is modeled using separate simulation software. Due to the diverse nature of these three areas, it was challenging to connect these simulation tools fully and to improve the fidelity of the simulations further. It is desirable to include all these aspects in one unified simulation environment. However, the existing commercial products have modeling limitations, which makes this approach impossible. An alternative method is the co-simulation approach to benefit from various simulation tools' capabilities to perform multidisciplinary simulations.

5.2. Limitations of the research

The QCD design is performed purely by utilizing numerical simulations. However, it is recommended that model tests of the concept be performed in addition to building a prototype of the design. These actions can help to fine-tune the numerical models and improve the validity of the research.

The QCD is in the initial stages of development, and the acceptable operational limits of this design are not quantified. This causes limitations to the design's operability. Based on the outcomes of this research, a systematic operability analysis is recommended.

CRediT authorship contribution statement

Behfar Ataei: Writing – review & editing, Writing – original draft, Visualization, Software, Methodology, Formal analysis, Conceptualization. **Zhengru Ren:** Writing – review & editing, Supervision, Software, Methodology, Conceptualization. **Karl Henning Halse:** Writing – review & editing, Supervision, Project administration, Funding acquisition, Conceptualization.

Declaration of competing interest

The authors declare that they have no known competing financial interests or personal relationships that could have appeared to influence the work reported in this paper.

Acknowledgments

This work was supported by the Research Council of Norway (RCN) through the Centre for Research-Based Innovation on Marine Operations (SFI MOVE, RCN-project 237929).

Data availability

Data will be made available on request.

References

- [1] Ritchie H, Rosado P, Roser M. Energy. Our World Data 2023. URL https://ourworldindata.org/energy.
- [2] Nations U. For a livable climate: Net-zero commitments must be backed by credible action. 2023, URL https://www.un.org/en/climatechange/net-zero-coalition.
- [3] Manwell JF, McGowan JG, Rogers AL. Wind energy explained: Theory, design and application. Wind energy explained. 2. Aufl.. New York: Wiley; 2010.
- [4] Ren Z, Verma AS, Li Y, Teuwen JJ, Jiang Z. Offshore wind turbine operations and maintenance: A state-of-the-art review. Renew Sustain Energy Rev 2021;144:110886. http://dx.doi.org/10.1016/j.rser.2021.110886, URL https://www.sciencedirect.com/science/article/pii/S1364032121001805.
- [5] NTNU. SFI move marine operations. 2023, URL https://www.ntnu.edu/move.
- [6] Mantey SK, Zhang Y, Jiang J, Amponsah E, Wang Z. Numerical model of cumulative damage evolution of offshore wind turbine grouted connection under cyclic axial load. Ocean Eng 2023;280:114520. http://dx.doi.org/10.1016/j.oceaneng.2023.114520, URL https://www.sciencedirect.com/science/article/pii/S0029801823009046.
- [7] Mantey SK, Zhang Y, Jiang J, Amponsah E, Wang Z. Fatigue damage development of grouted connection under varying cyclic loading. Appl Ocean Res 2022;127:103317. http://dx.doi.org/10.1016/j.apor.2022.103317, URL https://www.sciencedirect.com/science/article/pii/S0141118722002504.
- [8] DNV. DNV-ST-0126 support structures for wind turbines. 2021.
- [9] Chaki S, Corneloup G, Lillamand I, Walaszek H. Combination of longitudinal and transverse ultrasonic waves for in situ control of the tightening of bolts. J Press Vessel Technol 2006;129(3):383–90. http://dx.doi.org/10.1115/1.2748821, arXiv:https://asmedigitalcollection.asme.org/pressurevesseltech/article-pdf/129/3/383/5640042/383_1.pdf.

B. Ataei et al.

- [10] Cabboi A, Kamphuis T, van Veldhuizen E, Segeren M, Hendrikse H. Vibration-assisted decommissioning of a slip joint: Application to an offshore wind turbine. Mar Struct 2021;76:102931. http://dx.doi.org/10.1016/j.marstruc.2020.102931, URL https://www.sciencedirect.com/science/article/pii/ \$0951833920302215
- [11] Ataei B, Yuan S, Ren Z, Halse KH. Effects of structural flexibility on the dynamic responses of low-height lifting mechanism for offshore wind turbine installation. Mar Struct 2023;89:103399. http://dx.doi.org/10.1016/j.marstruc.2023.103399, URL https://www.sciencedirect.com/science/article/pii/S0951833923000321.
- [12] Sintef. Sima. 2023, URL https://www.sintef.no/en/software/sima/.
- [13] Orcina. OrcaFlex world-leading software that goes beyond expectation. 2023, URL https://www.orcina.com/orcaflex/.
- [14] Ren Z, Jiang Z, Skjetne R, Gao Z. Development and application of a simulator for offshore wind turbine blades installation. Ocean Eng 2018;166:380–95. http://dx.doi.org/10.1016/j.oceaneng.2018.05.011, URL https://www.sciencedirect.com/science/article/pii/S0029801818307224.
- [15] Ren Z, Verma AS, Ataei B, Halse KH, Hildre HP. Model-free anti-swing control of complex-shaped payload with offshore floating cranes and a large number of lift wires. Ocean Eng 2021;228:108868. http://dx.doi.org/10.1016/j.oceaneng.2021.108868, URL https://www.sciencedirect.com/science/article/pii/ S0029801821003036
- [16] Concepts and applications of finite element analysis, fourth ed., New York: Wiley; 2002.
- [17] Verma AS, Jiang Z, Vedvik NP, Gao Z, Ren Z. Impact assessment of a wind turbine blade root during an offshore mating process. Eng Struct 2019;180:205–22. http://dx.doi.org/10.1016/j.engstruct.2018.11.012, URL https://www.sciencedirect.com/science/article/pii/S0141029618315657.
- [18] Haris S, Amdahl J. Analysis of ship-ship collision damage accounting for bow and side deformation interaction. Mar Struct 2013;32:18–48. http://dx.doi.org/10.1016/j.marstruc.2013.02.002, URL https://www.sciencedirect.com/science/article/pii/S0951833913000166.
- [19] Moe OH, Sha Y, Veie J, rgen Amdahl J. Analysis of tether anchored floating suspension bridge subjected to large ship collisions. Procedia Eng 2017;199:2488–93. http://dx.doi.org/10.1016/j.proeng.2017.09.413, X International Conference on Structural Dynamics, EURODYN 2017.URL https://www.sciencedirect.com/science/article/pii/S187770581733905X.
- [20] Sha Y, rgen Amdahl J, rum CD. Numerical and analytical studies of ship deckhouse impact with steel and RC bridge girders. Eng Struct 2021;234:111868. http://dx.doi.org/10.1016/j.engstruct.2021.111868, URL https://www.sciencedirect.com/science/article/pii/S0141029621000183.
- [21] Yu Z, Amdahl J, Kristiansen D, Bore PT. Numerical analysis of local and global responses of an offshore fish farm subjected to ship impacts. Ocean Eng 2019;194:106653. http://dx.doi.org/10.1016/j.oceaneng.2019.106653, URL https://www.sciencedirect.com/science/article/pii/S0029801819307735.
- [22] Zhang Y, Hu Z, Ng C, Jia C, Jiang Z. Dynamic responses analysis of a 5 MW spar-type floating wind turbine under accidental ship-impact scenario. Mar Struct 2021;75:102885. http://dx.doi.org/10.1016/j.marstruc.2020.102885, URL https://www.sciencedirect.com/science/article/pii/S0951833920301787.
- [23] Song M, Jiang Z, Yuan W. Numerical and analytical analysis of a monopile-supported offshore wind turbine under ship impacts. Renew Energy 2021;167:457–72. http://dx.doi.org/10.1016/j.renene.2020.11.102, URL https://www.sciencedirect.com/science/article/pii/S0960148120318541.
- [24] Bilgili M, Alphan H. Global growth in offshore wind turbine technology. Clean Technol Environ Policy 2022;24:2215–27. http://dx.doi.org/10.1007/s10098-022-02314-0.
- [25] MathWorks. Simulink. 2023, URL https://se.mathworks.com/products/simulink.html.
- [26] Equinor. Hywind Scotland. 2017, URL https://www.equinor.com/en/what-we-do/floating-wind/hywind-scotland.html.
- [27] Liu T, Halse KH, Leira BJ, Jiang Z. Comparative study of the mating process for a spar-type floating wind turbine using two alternative installation vessels. Appl Ocean Res 2023;132:103452. http://dx.doi.org/10.1016/j.apor.2022.103452, URL https://www.sciencedirect.com/science/article/pii/S0141118722003819.
- [28] Bak C, Zahle F, Bitsche R, Kim T, Yde A, Henriksen LC, Hansen M, Natarajan A. Description of the DTU 10 MW Reference Wind Turbine. DTU Wind Energy; 2013.
- [29] Faltinsen OM. Sea loads on ships and offshore structures. Cambridge ocean technology series, Cambridge: Cambridge University Press; 1990.
- [30] Systèmes D. Why abagus unified fea?. 2023, URL https://www.3ds.com/products-services/simulia/products/abagus/.
- [31] Systèmes D. Abaqus 2022 user manual, hourglass stiffness. 2022.
- [32] Wang GS, A Study of Dynamic Properties of S355J2 Steel and Y925 Tungsten Alloy, FOI; 2021.
- [33] Moulas D, Shafiee M, Mehmanparast A. Damage analysis of ship collisions with offshore wind turbine foundations. Ocean engineering 2017;143:149-62.
- [34] Systèmes D. Abaqus 2022 user manual, element integration point variables. 2022.
- [35] Hong S, Zhang H, Nord TS, Halse KH. Effect of fender system on the dynamic response of onsite installation of floating offshore wind turbines. Ocean Eng 2022;259:111830. http://dx.doi.org/10.1016/j.oceaneng.2022.111830, URL https://www.sciencedirect.com/science/article/pii/S0029801822011738.
- [36] TRELLEBORG. Marine protection plates. 2024, URL https://www.trelleborg.com/en/marine-and-infrastructure/products-solutions-and-services/marine/marine-fenders/fixed-fenders/marine-protection-plates.